8

Grid Synchronization in Three-Phase Power Converters

8.1 Introduction

One of the lessons learned from the intensive research conducted on distributed power systems during last few years is that the electricity networks of the future will be based to a large extent on new power electronics and ICT applications, some of which have already been in use in other sectors of industry for decades [1]. This implies that grid-connected power converters applied in distributed power generation systems should be carefully designed and controlled in order to achieve even better performance than the conventional power plants they replace. One of the most important aspects to consider in the control of power converters connected to electrical grids is the proper synchronization with the three-phase utility voltages. This three-phase synchronization is not just a matter of multiplying by three the synchronization system used in single-phase applications, since the three phases of a three-phase system do not work autonomously but do it in a coordinated way, keeping particular relationships in terms of phase shifting and phase sequencing. Therefore, the three-phase voltage should be understood as a vector consisting of three voltage components, which provides the capability of generating and consuming power in a three-phase system.

The module and the rotation speed of the three-phase grid voltage vector keep constant when balanced sinusoidal waveforms are present in the three phases of the system – with equal amplitude, frequency and relative phase shifting. As shown in Figure 8.1, under such ideal operating conditions, the voltage vector describes a circular locus on a Cartesian plane, generally known as the $\alpha\beta$ plane.

In power systems, this rotating voltage vector is mainly supplied by big synchronous generators, and the electrical equipments located at the transmission, distribution and utilization levels are designed assuming that such a voltage vector has both a constant module and a constant positive rotation speed. In practice, however, there are multiple nonidealities in power systems that originate disturbances on the three-phase voltage vector. These voltage disturbances can be classified according to their harmonic spectrum, duration and amplitude

Grid Converters for Photovoltaic and Wind Power Systems Remus Teodorescu, Marco Liserre and Pedro Rodríguez
 ISBN: 978-0-470-05751-3

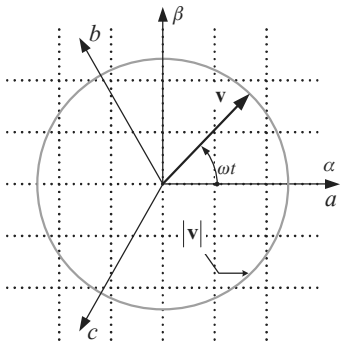

$$\mathbf{v}_{abc} = \begin{bmatrix} v_a \\ v_b \\ v_c \end{bmatrix} = V \begin{bmatrix} \cos(\omega t + \phi) \\ \cos(\omega t - \frac{2\pi}{3} + \phi) \\ \cos(\omega t + \frac{2\pi}{3} + \phi) \end{bmatrix}$$

$$|\mathbf{v}| = \sqrt{v_a^2 + v_b^2 + v_c^2} = \sqrt{\frac{3}{2}} V$$

Figure 8.1 Ideal three-phase voltage vector

and give rise to undesirable effects on electrical equipments, such as resonances, increasing power losses or premature ageing [2].

A grid-connected power converter is particularly sensitive to voltage disturbances since its control system might lose controllability on the power signals under such distorted operating conditions, which could trip any of its protection systems or might even destroy the power converter. Moreover, a power converter can interact with the grid at the point of common coupling in order to attenuate the voltage disturbances and reduce their undesirable effects. For these reasons, the voltage vector disturbances should be properly detected by the synchronization system, and the control system of the power converter should react to both ride-through such operating conditions and provide some support to the grid.

In the case where the voltage vector at the connection point of the power converter is distorted by high-order harmonics with reasonable amplitude, the detection system bandwidth can be reduced in order to cancel out the effect of these harmonics on the output. Despite this bandwidth reduction, the detection system should still operate satisfactorily in the presence of slow voltage fluctuations. In the case where the voltage vector is unbalanced, the bandwidth reduction is not an acceptable solution since the overall dynamic performance of the detection system would become unsatisfactorily deficient. In such a case, the sequence components of the unbalanced voltage vector should be identified by using specific detection techniques and passed as inputs to the control system to react accordingly to such voltage disturbance.

Therefore, grid synchronization of three-phase power converters entails the usage of advanced detection systems, specially designed to both reject high-order harmonics and identify the sequence components of the voltage vector in a fast and precise way. Particularly, the real-time detection of the sequence components of the voltage vector in three-phase networks is an essential issue in the control of distributed generation and storage systems, flexible AC transmission systems (FACTS), power line conditioners and uninterruptible power supplies (UPS) [3, 4]. In such systems, the magnitude and phase angle of the positive- and negative-sequence voltage components are generally used for the synchronization of the converter output variables, calculation of the power flow or transformation of stationary variables into rotating reference frames [5–7].

This chapter presents some three-phase synchronization systems suitable to be applied under unbalanced and distorted grid operating conditions.

8.2 The Three-Phase Voltage Vector under Grid Faults

Three-phase voltages can become unbalanced and distorted because of the effect of nonlinear loads and transient grid faults. Ideally, power converters used in distributed generation should be properly synchronized with the grid under such adverse operating conditions to stay actively connected, supporting the grid services (voltage/frequency) and keeping up generation. The faulty three-phase voltages can be generically understood as a summation of unbalanced harmonic components. Therefore, in a general way, the three-phase voltage vector can be written as

$$\boldsymbol{v}_{abc} = \begin{bmatrix} v_a \\ v_b \\ v_c \end{bmatrix} = \sum_{n=1}^{\infty} \left(\boldsymbol{v}_{abc}^{+n} + \boldsymbol{v}_{abc}^{-n} + \boldsymbol{v}_{abc}^{0n} \right), \tag{8.1}$$

where

$$\boldsymbol{v}_{abc}^{+n} = V^{+n} \begin{bmatrix} \cos(n\omega t + \phi^{+n}) \\ \cos(n\omega t - \frac{2\pi}{3} + \phi^{+n}) \\ \cos(n\omega t + \frac{2\pi}{3} + \phi^{+n}) \end{bmatrix} \tag{8.2.a}$$

$$\boldsymbol{v}_{abc}^{-n} = V^{-n} \begin{bmatrix} \cos(n\omega t + \phi^{-n}) \\ \cos(n\omega t + \frac{2\pi}{3} + \phi^{-n}) \\ \cos(n\omega t - \frac{2\pi}{3} + \phi^{-n}) \end{bmatrix} \tag{8.2.b}$$

$$\boldsymbol{v}_{abc}^{0n} = V^{0n} \begin{bmatrix} \cos(n\omega t + \phi^{0n}) \\ \cos(n\omega t + \phi^{0n}) \\ \cos(n\omega t + \phi^{0n}) \end{bmatrix} \tag{8.2.c}$$

In (8.1) and (8.2), superscripts $+n$, $-n$ and $0n$ respectively represent the positive-, negative- and zero-sequence components of the nth harmonic of the voltage vector $\boldsymbol{v}$.

Distributed generators are usually linked to three-phase networks by using a three-wire connection and hence they do not inject zero-sequence current into the grid. Thus, the zero-sequence component of the voltage vector will be intentionally ignored in the equations describing the synchronization systems presented in this chapter since it is not necessary to synchronize any current with such a zero-sequence voltage component. Nonetheless, if necessary, the zero-sequence component could be easily extracted from the voltage vector by applying the *Clarke* transformation, defined by (A.14) in Appendix A, and its characteristic module and phase angle can be determined by using any of the single-phase synchronization systems presented in Chapter 4. Moreover, three-phase power converters used in WT and PV systems generally inject positive-sequence currents at the fundamental frequency into the grid and only intentionally inject negative-sequence and harmonics currents in unusual cases, i.e. either avoiding power oscillations to protect the power converter or injecting unbalanced reactive currents to compensate the unbalanced grid voltage at the point of common coupling. Therefore, the correct detection of the positive-sequence component at the fundamental frequency of the three-phase grid voltage can be considered as the main task of the synchronization system of a grid-connected three-phase power converter.

In a general form, a positive-sequence voltage vector at the fundamental frequency interacting with either a positive- or negative-sequence nth-order component can be expressed by

$$\boldsymbol{v}_{abc} = \boldsymbol{v}_{abc}^{+1} + \boldsymbol{v}_{abc}^{n} = V^{+1}\begin{bmatrix} \cos(\omega t) \\ \cos(\omega t - \frac{2\pi}{3}) \\ \cos(\omega t + \frac{2\pi}{3}) \end{bmatrix} + V^{n}\begin{bmatrix} \cos(n\omega t) \\ \cos(n\omega t - \frac{2\pi}{3}) \\ \cos(n\omega t + \frac{2\pi}{3}) \end{bmatrix} \tag{8.3}$$

where $n > 0$ means a positive-sequence component and $n < 0$ a negative-sequence one. The voltage vector of (8.3) can be expressed on the Cartesian $\alpha\beta$ stationary reference frame by using a reduced version of the *Clarke* transformation, resulting in

$$\boldsymbol{v}_{\alpha\beta} = \begin{bmatrix} v_\alpha \\ v_\beta \end{bmatrix} = \left[T_{\alpha\beta}\right] \cdot \boldsymbol{v}_{abc} = \sqrt{\frac{3}{2}} V^{+1}\begin{bmatrix} \cos(\omega t) \\ \sin(\omega t) \end{bmatrix} + \sqrt{\frac{3}{2}} V^{n}\begin{bmatrix} \cos(n\omega t) \\ \sin(n\omega t) \end{bmatrix} \tag{8.4}$$

where

$$\left[T_{\alpha\beta}\right] = \sqrt{\frac{2}{3}}\begin{bmatrix} 1 & -\frac{1}{2} & -\frac{1}{2} \\ 0 & \frac{\sqrt{3}}{2} & -\frac{\sqrt{3}}{2} \end{bmatrix} \tag{8.5}$$

The voltage vector of (8.3) can also be expressed on a Cartesian dq rotating reference frame by using the *Park* transformation as

$$\boldsymbol{v}_{dq} = \begin{bmatrix} v_d \\ v_q \end{bmatrix} = \left[T_{dq}\right] \cdot \boldsymbol{v}_{\alpha\beta} = \sqrt{\frac{3}{2}} V^{+1}\begin{bmatrix} \cos(\omega t - \theta') \\ \sin(\omega t - \theta') \end{bmatrix} + \sqrt{\frac{3}{2}} V^{n}\begin{bmatrix} \cos(n\omega t - \theta') \\ \sin(n\omega t - \theta') \end{bmatrix} \tag{8.6}$$

where

$$\left[T_{dq}\right] = \begin{bmatrix} \cos(\theta') & \sin(\theta') \\ -\sin(\theta') & \cos(\theta') \end{bmatrix} \tag{8.7}$$

with θ' the angular position of the dq rotating reference frame.

As an illustrative example, Figure 8.2 shows the evolution of the three-phase voltage vector of (8.3) in two different cases. Figure 8.2(a) shows the interaction of the fundamental frequency positive-sequence component with a fundamental frequency negative-sequence component ($n = -1$), whereas Figure 8.2(b) shows the interaction of the fundamental frequency positive-sequence component with a fifth harmonic negative-sequence component ($n = -5$).

Assuming that the dq reference frame rotates synchronously with the positive-sequence voltage vector, with the d axis in the same direction as the positive-sequence voltage vector $\boldsymbol{v}^{+1}$, i.e. with $\theta' = \omega t$, the expression of (8.6) gives rise to

$$\boldsymbol{v}_{dq} = \sqrt{\frac{3}{2}} V^{+1}\begin{bmatrix} 1 \\ 0 \end{bmatrix} + \sqrt{\frac{3}{2}} V^{n}\begin{bmatrix} \cos\left((n-1)\,\omega t\right) \\ \sin\left((n-1)\,\omega t\right) \end{bmatrix} \tag{8.8}$$

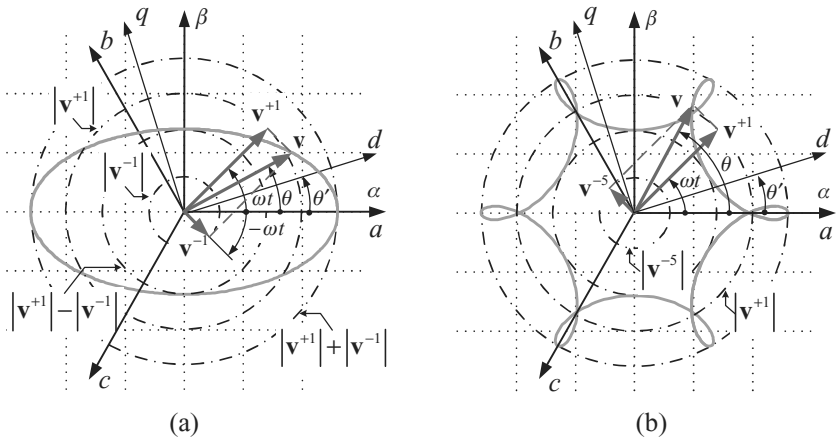

Figure 8.2 Locus of (a) an unbalanced and (b) a distorted voltage vector

From (8.8), the module and angular position of the three-phase voltage vector, $|\boldsymbol{v}|$ and θ respectively are given by

$$|\boldsymbol{v}| = \sqrt{v_\alpha^2 + v_\beta^2} = \sqrt{\frac{3}{2}\left[\left(V^{+1}\right)^2 + \left(V^n\right)^2 + 2V^{+1}V^n \cos\left((n-1)\,\omega t\right)\right]} \tag{8.9}$$

$$\theta = \tan^{-1}\frac{v_\beta}{v_\alpha} = \omega t + \tan^{-1}\left(\frac{v_q}{v_d}\right) = \omega t + \tan^{-1}\left[\frac{V^n \sin\left((n-1)\,\omega t\right)}{V^{+1} + V^n \cos\left((n-1)\,\omega t\right)}\right] \tag{8.10}$$

Equations (8.9) and (8.10) are evidence that the compound voltage vector $\boldsymbol{v}$ has neither constant module nor rotational frequency. Moreover, these equations show that both the amplitude and the angular position of the positive-sequence component cannot be extracted by just filtering the detected module and phase angle of the compound voltage vector $\boldsymbol{v}$.

As an example, Figure 8.3(a) shows the phase voltage waveforms of a three-phase system affected by a phase-to-phase grid fault. Just the positive- and negative-sequence components are considered in this example, being $V^{+1} = 0.75$ p.u. and $V^{-1} = 0.25$ p.u. (it is assumed here that the pre-fault voltage amplitude is equal to 1 p.u.). Therefore, the module and angular position of the voltage vector during the grid fault are given by

$$|\boldsymbol{v}| = \sqrt{0.9375 + 0.5625\cos\left(2\omega t\right)} \tag{8.11}$$

$$\theta = \omega t + \tan^{-1}\left[\frac{0.25\sin\left(-2\omega t\right)}{0.75 + 0.25\cos\left(2\omega t\right)}\right] \tag{8.12}$$

Figure 8.3(b) shows the locus described by the voltage vector normalized with respect to the pre-fault vector module. In this figure, the instantaneous value of the angular frequency of the voltage vector, $\mathrm{d}\theta/\mathrm{d}t$, has been represented on a vertical axis, orthogonal to the $\alpha\beta$ plane. It can

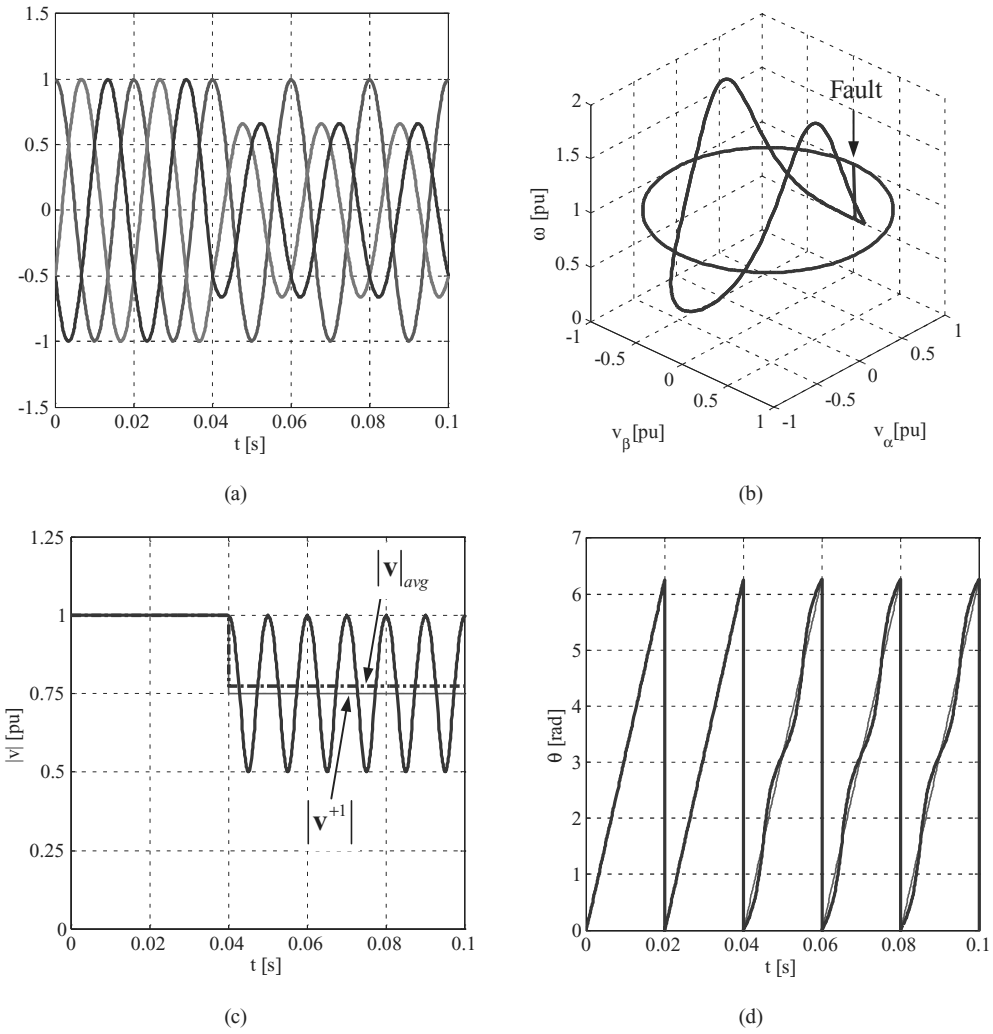

Figure 8.3 Space vector evolution in a phase-to-phase grid fault

be appreciated in this figure how the voltage vector locus changes from a circle to a completely different shape once the fault happens. However, the projection of this three-dimensional shape on the $\alpha\beta$ plane matches the ellipse plotted in Figure 8.2(a). This figure highlights that the instantaneous angular frequency of the voltage vector is not a constant during the grid fault, which should be taken into account when a three-phase synchronization system is designed.

Figure 8.3(c) shows the evolution of the voltage vector module $|\boldsymbol{v}|$, normalized with respect to the pre-fault vector module. The average value of the voltage vector module during the grid fault, $|\boldsymbol{v}|_{avg}$, is plotted by a dashed line, whereas the module of the positive-sequence voltage vector, $|\boldsymbol{v}^{+1}|$, is plotted by a thin continuous line. Figure 8.3(d) shows the evolution of

the voltage vector phase angle θ. Both figures show that the information about the positive-sequence voltage vector $\boldsymbol{v}^{+1}$ cannot be properly obtained by just applying conventional filtering techniques to the module and phase-angle signals of the compound vector $\boldsymbol{v}$.

8.2.1 Unbalanced Grid Voltages during a Grid Fault

Before presenting some solutions for detecting the sequence components of an unbalanced voltage vector, an example of how such unbalanced voltages are generated during a grid fault will be presented here. The analysis procedure presented in the following can be applied to any kind of grid fault to obtain its characteristic parameters (three-phase, three-phase to ground, phase to ground, etc.). Nevertheless, a more detailed explanation about this topic can be found in the literature [8–10].

The phase-to-phase grid fault that originated the unbalanced waveforms of Figure 8.3(a) can be represented by the circuit of Figure 8.4, where it is assumed that the line impedance is equal for all three phases and the voltage supplied by the three-phase generator is sinusoidal, balanced with positive-sequence components, at the fundamental frequency.

The phase voltages and current in the faulty lines of Figure 8.4 verify that

$$v_{b'} = \boldsymbol{v}_{c'}; \qquad i_{b'} = -i_{c'}; \qquad i_{a'} = 0 \tag{8.13}$$

From (8.13) and using phasors, the positive-, negative- and zero-sequence voltage components at the fault point, $\vec{V}_{a'}^{+}$, $\vec{V}_{a'}^{-}$, $\vec{V}_{a'}^{0}$, can be calculated by equation (A.1) of Appendix A, resulting in

$$\mathbf{V}_{+-0(a')} = \begin{bmatrix} \vec{V}_{a'}^{+} \\ \vec{V}_{a'}^{-} \\ \vec{V}_{a'}^{0} \end{bmatrix} = \frac{1}{3}\begin{bmatrix} 1 & \alpha & \alpha^2 \\ 1 & \alpha^2 & \alpha \\ 1 & 1 & 1 \end{bmatrix}\begin{bmatrix} \vec{V}_{a'} \\ \vec{V}_{b'} \\ \vec{V}_{c'} \end{bmatrix} = \frac{1}{3}\begin{bmatrix} \vec{V}_{a'} - \vec{V}_{b'} \\ \vec{V}_{a'} - \vec{V}_{b'} \\ \vec{V}_{a'} + 2\vec{V}_{b'} \end{bmatrix} \tag{8.14}$$

where $\alpha = e^{j2\pi/3} = 1\angle 120^\circ$ is the *Fortescue* operator [11]. Voltage phasors of (8.14) indicate that the positive- and negative-sequence voltage components at the fault point are equal, i.e. $\vec{V}_{a'}^{+} = \vec{V}_{a'}^{-}$.

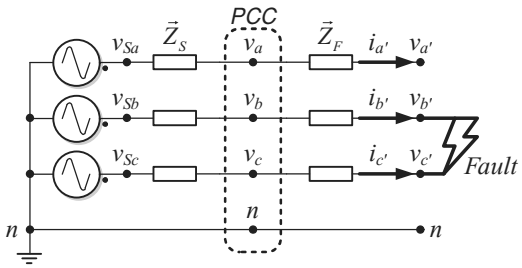

Figure 8.4 Three-phase circuit of a phase-to-phase grid fault

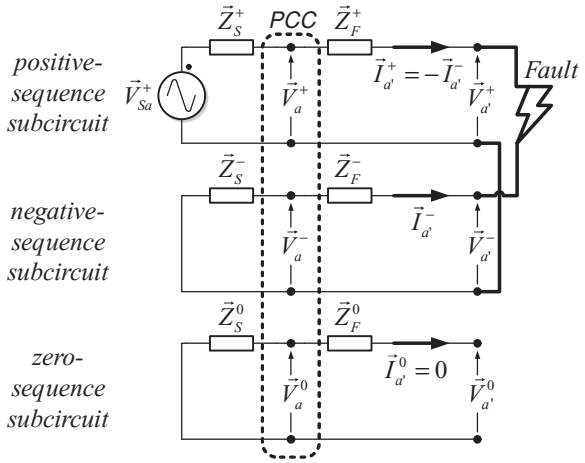

Figure 8.5 Sequence components based on the equivalent circuit of a phase-to-phase grid fault

Likewise, from (8.13), the positive-, negative- and zero-sequence components of the line currents during the grid fault are given by

$$\mathbf{I}_{+-0(a')} = \begin{bmatrix} \vec{I}_{a'}^{+} \\ \vec{I}_{a'}^{-} \\ \vec{I}_{a'}^{0} \end{bmatrix} = \frac{1}{3} \begin{bmatrix} 1 & \alpha & \alpha^2 \\ 1 & \alpha^2 & \alpha \\ 1 & 1 & 1 \end{bmatrix} \begin{bmatrix} \vec{I}_{a'} \\ \vec{I}_{b'} \\ \vec{I}_{c'} \end{bmatrix} = \frac{1}{\sqrt{3}} \begin{bmatrix} j\vec{I}_{b'} \\ -j\vec{I}_{b'} \\ 0 \end{bmatrix} \tag{8.15}$$

Current phasors of (8.15) indicate that the zero-sequence current component is equal to zero and, consequently, the addition of the positive- and negative-sequence current components are equal to zero as well, namely $\vec{I}_{a'}^{0} = 0$ and $\vec{I}_{a'}^{+} + \vec{I}_{a'}^{-} = 0$.

Once the relationships between the sequence components of voltages and currents during the grid fault are defined, the actual three-phase circuit of Figure 8.4 can be transformed into the equivalent circuits of Figure 8.5 based on the sequence components. In this figure, $\vec{V}_{Sa}^{+}$ represents the pre-fault voltage vector of the phase a, i.e. one of the three phase voltages of the positive-sequence balanced pre-fault voltage vector.

Assuming that the positive- and negative-sequence line impedances at the source side are equal, i.e. $\vec{Z}_S^{+} = \vec{Z}_S^{-} = \vec{Z}_S$, which is true in most cases, the circuit of Figure 8.5 gives rise to the following sequence voltages at the point of common coupling (PCC):

$$\vec{V}_a^{+} = \frac{\vec{Z}_S + \left(\vec{Z}_F^{+} + \vec{Z}_F^{-}\right)}{2\vec{Z}_S + \left(\vec{Z}_F^{+} + \vec{Z}_F^{-}\right)} \vec{V}_{Sa}^{+} \tag{8.16a}$$

$$\vec{V}_a^{-} = \frac{\vec{Z}_S}{2\vec{Z}_S + \left(\vec{Z}_F^{+} + \vec{Z}_F^{-}\right)} \vec{V}_{Sa}^{+} \tag{8.16b}$$

$$\vec{V}_a^{0} = 0 \tag{8.16c}$$

The severity of the grid fault seen from the PCC can be assessed by the dip parameter $\vec{D}$, which defines the relationship between the line impedances at the fault side and the source side, i.e.

$$\vec{D} = D\angle\rho_D = \frac{\left(\vec{Z}_F^+ + \vec{Z}_F^-\right)}{2\vec{Z}_S + \left(\vec{Z}_F^+ + \vec{Z}_F^-\right)} \tag{8.17}$$

It is worth highlighting here that the magnitude of the faulty voltage depends on the distance from the PCC to the fault point, namely it mainly depends on the module of $\vec{D}$. The difference in the phase angle between the pre-fault and the faulty voltage depends on the phase angle of $\vec{D}$. If the *X*/*R* ratio of the impedances at both sides of the PCC remains constant, i.e. if the phase angle of $\vec{Z}_S$ is equal to that of $\vec{Z}_F^+ + \vec{Z}_F^-$, there is no phase-angle jump between the pre-fault and the faulty voltage.

Substituting (8.17) in (8.16), the sequence voltages at the PCC can be written as

$$\mathbf{V}_{+-0(pcc)} = \begin{bmatrix} \vec{V}_a^+ \\ \vec{V}_a^- \\ \vec{V}_a^0 \end{bmatrix} = \frac{1}{2}\vec{V}_{Sa}^+ \begin{bmatrix} 1+\vec{D} \\ 1-\vec{D} \\ 0 \end{bmatrix} \tag{8.18}$$

From (8.18), the phase voltages at the PCC can be calculated by using equation (A.4) of Appendix A, resulting in

$$\mathbf{V}_{abc(pcc)} = \begin{bmatrix} \vec{V}_a \\ \vec{V}_b \\ \vec{V}_c \end{bmatrix} = \begin{bmatrix} 1 & 1 & 1 \\ \alpha^2 & \alpha & 1 \\ \alpha & \alpha^2 & 1 \end{bmatrix} \begin{bmatrix} \vec{V}_a^+ \\ \vec{V}_a^- \\ \vec{V}_a^0 \end{bmatrix} = \vec{V}_{Sa}^+ \begin{bmatrix} 1 \\ -\frac{1}{2} - \frac{\sqrt{3}}{2}\vec{D} \\ -\frac{1}{2} + \frac{\sqrt{3}}{2}\vec{D} \end{bmatrix} \tag{8.19}$$

In this example, the voltage phasors of (8.19) describe the unbalanced voltage waveforms of Figure 8.3(a), which are related to a phase-to-phase grid fault.

8.2.2 Transient Grid Faults, the Voltage Sags (Dips)

A voltage sag, also called a voltage dip, is a sudden reduction of the grid voltage at the PCC, generally between 10 and 90 % of the rated value, during a period lasting from half a cycle to a few seconds. Voltage sags usually happen as a consequence of short-circuits, faults to ground, transformers energizing and connection of large induction motors. Depending on both the type of grid fault and the transformer connections along the power lines, it is possible to distinguish between different types of voltage sags.

The definition of guidelines to classify voltage sags is a matter that remains under discussion still today [12]. The product $\vec{D}\vec{V}_{Sa}^+$ is known as the 'characteristic voltage' of the voltage sag and represents either the phase voltage in phase-to-ground faults or the line-to-line voltage in phase-to-phase faults. Likewise, the phase angle of $\vec{D}$ is known as the 'characteristic phase angle jump' of the voltage sag. Figure 8.6 shows four types of voltage sag resulting from

Sag type **A**. Three-phase fault and three-phase-to-ground fault

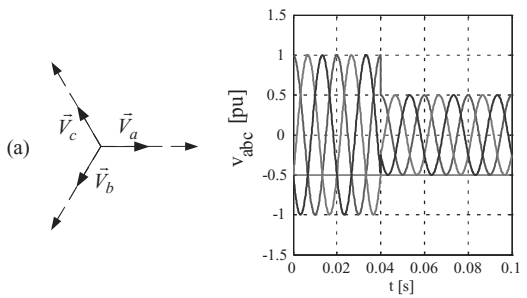

$$\begin{bmatrix}\vec{V}_a\\ \vec{V}_b\\ \vec{V}_c\end{bmatrix}=\begin{bmatrix}1\\ -\frac{1}{2}-j\frac{\sqrt{3}}{2}\\ -\frac{1}{2}+j\frac{\sqrt{3}}{2}\end{bmatrix}\vec{D}\vec{V}_{Sa}^{+},\qquad \begin{bmatrix}\vec{V}_a^{+}\\ \vec{V}_a^{-}\\ \vec{V}_a^{0}\end{bmatrix}=\begin{bmatrix}1\\ 0\\ 0\end{bmatrix}\vec{D}\vec{V}_{Sa}^{+},\qquad \vec{D}=\frac{\vec{Z}_F^{+}}{\vec{Z}_S+\vec{Z}_F^{+}}$$

Sag type **B**. Single-phase-to-ground fault

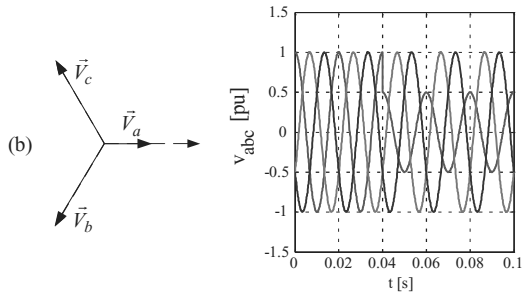

$$\begin{bmatrix}\vec{V}_a\\ \vec{V}_b\\ \vec{V}_c\end{bmatrix}=\begin{bmatrix}\vec{D}\\ -\frac{1}{2}-j\frac{\sqrt{3}}{2}\\ -\frac{1}{2}+j\frac{\sqrt{3}}{2}\end{bmatrix}\vec{V}_{Sa}^{+},\qquad \begin{bmatrix}\vec{V}_a^{+}\\ \vec{V}_a^{-}\\ \vec{V}_a^{0}\end{bmatrix}=\begin{bmatrix}\frac{1}{3}(2+\vec{D})\\ \frac{-1}{3}(1-\vec{D})\\ \frac{-1}{3}(1-\vec{D})\end{bmatrix}\vec{V}_{Sa}^{+},\qquad \vec{D}=\frac{\vec{Z}_F^{+}+\vec{Z}_F^{-}+\vec{Z}_F^{0}}{3\vec{Z}_S+\vec{Z}_F^{+}+\vec{Z}_F^{-}+\vec{Z}_F^{0}}$$

Sag type **C**. Phase-to-phase fault

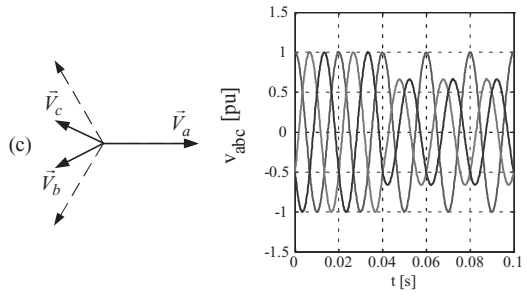

$$\begin{bmatrix}\vec{V}_a\\ \vec{V}_b\\ \vec{V}_c\end{bmatrix}=\begin{bmatrix}1\\ -\frac{1}{2}-j\frac{\sqrt{3}}{2}\vec{D}\\ -\frac{1}{2}+j\frac{\sqrt{3}}{2}\vec{D}\end{bmatrix}\vec{V}_{Sa}^{+},\qquad \begin{bmatrix}\vec{V}_a^{+}\\ \vec{V}_a^{-}\\ \vec{V}_a^{0}\end{bmatrix}=\begin{bmatrix}\frac{1}{2}(1+\vec{D})\\ \frac{1}{2}(1-\vec{D})\\ 0\end{bmatrix}\vec{V}_{Sa}^{+},\qquad \vec{D}=\frac{\vec{Z}_F^{+}+\vec{Z}_F^{-}}{2\vec{Z}_S+\vec{Z}_F^{+}+\vec{Z}_F^{-}}$$

Sag type **E**. Two-phase to ground fault

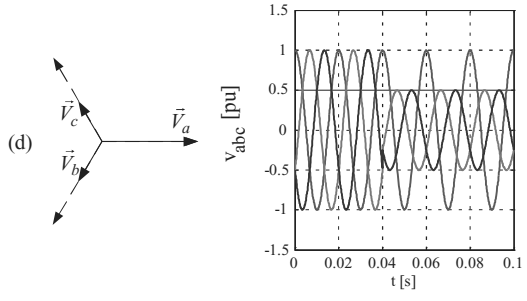

$$\begin{bmatrix}\vec{V}_a\\ \vec{V}_b\\ \vec{V}_c\end{bmatrix}=\begin{bmatrix}1\\ -\frac{1}{2}\vec{D}-j\frac{\sqrt{3}}{2}\vec{D}\\ -\frac{1}{2}\vec{D}+j\frac{\sqrt{3}}{2}\vec{D}\end{bmatrix}\vec{V}_{Sa}^{+},\qquad \begin{bmatrix}\vec{V}_a^{+}\\ \vec{V}_a^{-}\\ \vec{V}_a^{0}\end{bmatrix}=\begin{bmatrix}\frac{1}{3}(1+2\vec{D})\\ \frac{1}{3}(1-\vec{D})\\ \frac{1}{3}(1-\vec{D})\end{bmatrix}\vec{V}_{Sa}^{+},\qquad \vec{D}=\frac{\vec{Z}_F}{\vec{Z}_S+\vec{Z}_F}$$

Figure 8.6 Voltage sags due to grid faults in three-phase systems with $\vec{D}=0.5\angle 0^{\circ}$

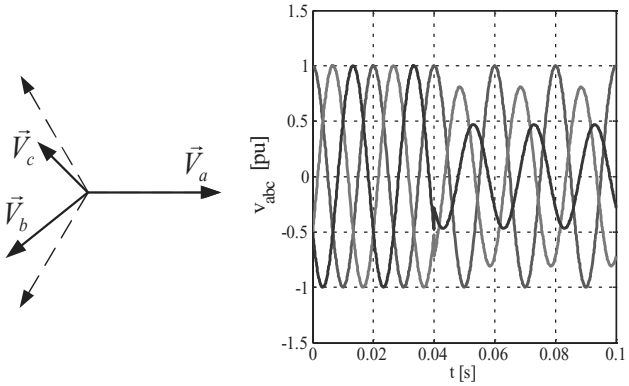

$$\begin{bmatrix} \vec{V}_a \\ \vec{V}_b \\ \vec{V}_c \end{bmatrix} = \begin{bmatrix} 1.0\angle 0^{\circ} \\ 0.81\angle -152^{\circ} \\ 0.48\angle 127^{\circ} \end{bmatrix},$$

$$\begin{bmatrix} \vec{V}_a^{+} \\ \vec{V}_a^{-} \\ \vec{V}_a^{0} \end{bmatrix} = \begin{bmatrix} 0.73\angle -9.9^{\circ} \\ 0.30\angle 23.8^{\circ} \\ 0 \end{bmatrix}.$$

Figure 8.7 Voltage sag type C with $\vec{D} = 0.5\angle -30^{\circ}$

different grid faults in which the characteristic phase angle jump was assumed equal to zero. In this figure, the voltage sags have been typified according to the nomenclature proposed in reference [8]. The characteristic parameters of the voltage sags of Figure 8.6 can be calculated by following a similar procedure to the one described in the previous example for a phase-to-phase fault. A more detailed explanation about this mathematical procedure can be found in reference [9].

There are many practical cases in which the *X*/*R* ratio of the impedances at both sides of the PCC of Figure 8.4 does not keep constant during a fault, which implies a phase-angle jump is different to zero. This is particularly true when the fault affects to power lines consisting of sections with different impedances, or when big induction motors are connected to the grid. In such a case, the voltage phasors during the grid fault lose the symmetry, shown by the sags of Figure 8.6. As an example, Figure 8.7 shows a voltage sag type C with $\vec{D} = 0.5\angle -30^{\circ}$.

8.2.3 Propagation of Voltage Sags

The type of sag experienced by a system connected to a given AC bus not only depends on the number of phases affected by the grid fault but it is also influenced by the transformers located in between the AC bus and the fault point. The amplitude and phase angle of the unbalanced voltage resulting from a given grid fault will be modified when propagated through regular three-phase transformers used in power systems, which will give rise to new types of voltage sags different to the ones shown in Figure 8.6. Moreover, the zero-sequence component, generally present in phase-to-ground faults, will be removed. As an example, Figure 8.8 shows how the line-to-line voltages of a sag type C applied to the primary of a *Dy* transformer are propagated to the secondary winding with different voltage amplitudes and phase angles, which results in a new type of voltage sag (type D).

To identify the different types of voltage sag existing in a generic distribution system, voltage on the buses of a power line like the one shown in Figure 8.9 are analysed in this section. In this analysis, three possible points of common coupling (PCC_1, PCC_2 and PCC_3) are considered, which result from the cascade connection of two *Dy* transformers. An analysis

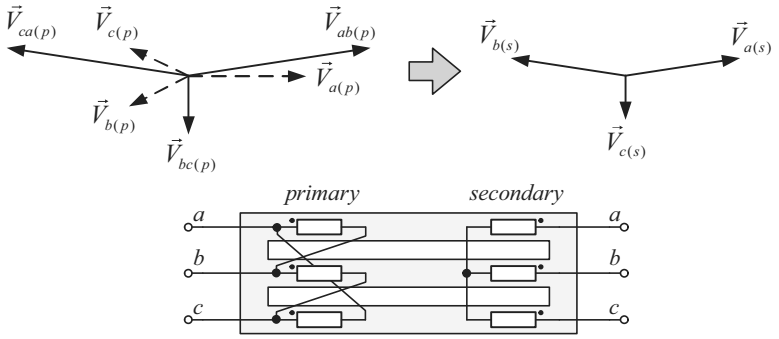

Figure 8.8 Propagation of a voltage sag type C ($\vec{D} = 0.5\angle -0^{\circ}$) through a *Dy* transformer

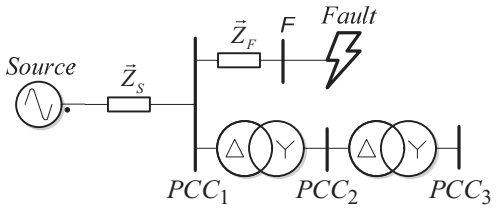

Figure 8.9 Voltage sag propagation along three points of common coupling (PCC_1, PCC_2 and PCC_3) in a power line with two cascade-connected *Dy* transformers

of the voltages measured on PCC_2 and PCC_3 allows three new types of voltage sags (types D, F and G) to be identified from the original voltage sags (types A, B, C and E) existing on bus PCC_1 as a consequence of different types of faults occurred at bus F.

The relationship between the different types of voltage sag is summarized in Table 8.1. The sequence components and phase-voltages of the voltage sag types D, F and G are shown in Figure 8.10.

Table 8.1 Propagation of voltage sags through *Dy* transformers

	Point of common coupling		
Fault type	PCC_1	PCC_2	PCC_3
Three-phase/three-phase to ground	A	A	A
Single-phase to ground	B	C	D
Two-phase	C	D	C
Two-phase to ground	E	F	G

Sag type **D**. Propagation of a sag type **C**

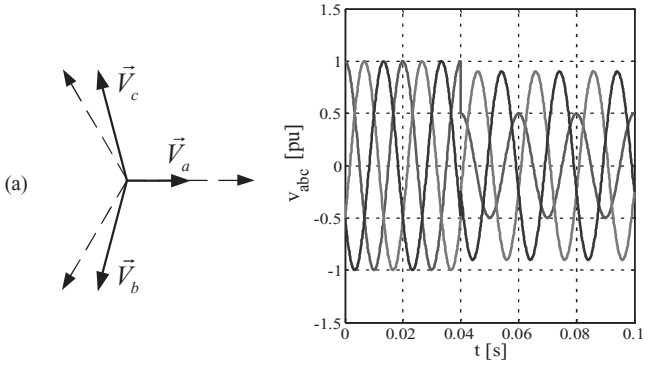

$$\begin{bmatrix}\vec{V}_a\\ \vec{V}_b\\ \vec{V}_c\end{bmatrix}=\begin{bmatrix}\vec{D}\\ -\frac{1}{2}\vec{D}-j\frac{\sqrt{3}}{2}\\ -\frac{1}{2}\vec{D}+j\frac{\sqrt{3}}{2}\end{bmatrix}\vec{V}_{Sa}^{+},\qquad \begin{bmatrix}\vec{V}_a^{+}\\ \vec{V}_a^{-}\\ \vec{V}_a^{0}\end{bmatrix}=\begin{bmatrix}\frac{1}{2}(1+\vec{D})\\ -\frac{1}{2}(1-\vec{D})\\ 0\end{bmatrix}\vec{V}_{Sa}^{+}$$

Sag type **F**. Propagation of a sag type **E**

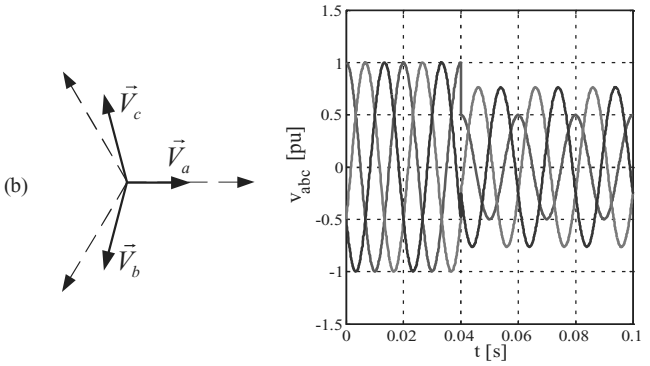

$$\begin{bmatrix}\vec{V}_a\\ \vec{V}_b\\ \vec{V}_c\end{bmatrix}=\begin{bmatrix}\vec{D}\\ -\frac{1}{2}\vec{D}-j(\frac{2+\vec{D}}{\sqrt{12}})\\ -\frac{1}{2}\vec{D}+j(\frac{2+\vec{D}}{\sqrt{12}})\end{bmatrix}\vec{V}_{Sa}^{+},\qquad \begin{bmatrix}\vec{V}_a^{+}\\ \vec{V}_a^{-}\\ \vec{V}_a^{0}\end{bmatrix}=\begin{bmatrix}\frac{1}{3}(1+2\vec{D})\\ \frac{-1}{3}(1-\vec{D})\\ 0\end{bmatrix}$$

Sag type **G**. Propagation of a sag type **F**

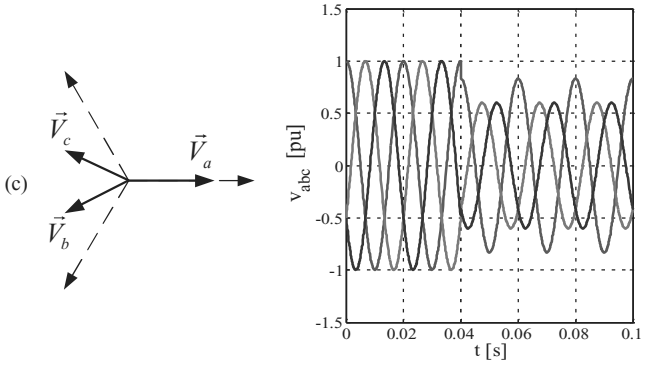

$$\begin{bmatrix}\vec{V}_a\\ \vec{V}_b\\ \vec{V}_c\end{bmatrix}=\begin{bmatrix}\frac{1}{3}(2+\vec{D})\\ -\frac{2+\vec{D}}{6}-j\frac{\sqrt{3}}{2}\vec{D}\\ -\frac{2+\vec{D}}{6}+j\frac{\sqrt{3}}{2}\vec{D}\end{bmatrix}\vec{V}_{Sa}^{+},\qquad \begin{bmatrix}\vec{V}_a^{+}\\ \vec{V}_a^{-}\\ \vec{V}_a^{0}\end{bmatrix}=\begin{bmatrix}\frac{1}{3}(1+2\vec{D})\\ \frac{1}{3}(1-\vec{D})\\ 0\end{bmatrix}\vec{V}_{Sa}^{+}$$

Figure 8.10 Voltage sags due to the propagation of grid faults in three-phase systems with $\vec{D}=0.5\angle 0^{\circ}$

8.3 The Synchronous Reference Frame PLL under Unbalanced and Distorted Grid Conditions

The most extended technique used for frequency-insensitive grid synchronization in three-phase systems is the PLL based on the synchronous reference frame (SRF-PLL) [13]. The conventional SRF-PLL translates the three-phase voltage vector from the *abc* natural reference frame to the *dq* rotating reference frame by using Park's transformation $[T_\theta]$, as shown in Figure 8.11. The angular position of this *dq* reference frame is controlled by a feedback loop that regulates the q component to zero. As shown in (8.20), the $[T_\theta]$ transformation in this PLL has been rescaled by using a 2/3 factor in order to detect the amplitude of the sinusoidal input signal instead of the module of the input voltage vector. Therefore, in the steady state, the d component depicts the amplitude of the sinusoidal positive-sequence input voltage (V^{+1}) and its phase angle is determined by the output of the feedback loop (θ').

$$\begin{bmatrix} v_d \\ v_q \end{bmatrix} = [T_\theta] \begin{bmatrix} v_a \\ v_b \\ v_c \end{bmatrix}, [T_\theta] = \frac{2}{3} \begin{bmatrix} \cos(\theta') & \cos(\theta' - \frac{2\pi}{3}) & \cos(\theta' + \frac{2\pi}{3}) \\ -\sin(\theta') & -\sin(\theta' - \frac{2\pi}{3}) & -\sin(\theta' + \frac{2\pi}{3}) \end{bmatrix} \tag{8.20}$$

$$[T_\theta] = \left[T_{dq}\right] \cdot \left[T_{\alpha\beta}\right], \left[T_{dq}\right] = \begin{bmatrix} \cos(\theta') & \sin(\theta') \\ -\sin(\theta') & \cos(\theta') \end{bmatrix}, \left[T_{\alpha\beta}\right] = \frac{2}{3} \begin{bmatrix} 1 & -\frac{1}{2} & -\frac{1}{2} \\ 0 & \frac{\sqrt{3}}{2} & -\frac{\sqrt{3}}{2} \end{bmatrix} \tag{8.21}$$

Under ideal grid conditions, i.e. when the grid voltage is not affected by either harmonic distortion or unbalances, setting a high bandwidth for the SRF-PLL feedback loop yields a fast and precise detection of the phase angle and amplitude of the grid voltage. Column (a) of Figure 8.12 shows some waveforms illustrating the response of an SRF-PLL, tuned with a high gain, i.e. a high bandwidth, in the presence of a voltage sag type A. As shown in this figure, the SRF-PLL almost instantaneously detects the amplitude and phase angle of the balanced input voltage vector by making $v_q = 0$. Column (b) of Figure 8.12 shows the response of the SRF-PLL when the voltage sag type A is polluted by a fifth-order harmonic ($V^{-5} = 0.1V^{+1}$). In this case, the SRF-PLL makes a small error in tracking the instantaneous position of the input voltage vector and consequently $v_q \neq 0$. This is in fact an advantage, since the PLL automatically will reduce the effect of the fifth-order harmonic on the angular position of the *dq* reference frame. Hence, the average value of the voltage on the d axis will match the amplitude of the positive-sequence fundamental voltage, i.e. $\bar{v}_d = V^{+1}$. Therefore, it can be concluded that a slight reduction in the PLL bandwidth improves its response, almost completely rejecting the effect of high-order harmonics on the PLL output signals. Column (c) of Figure 8.12 shows the response of an SRF-PLL when the grid voltage experienced a sag type C with $\vec{V}_a^{+1} = 0.75\angle 0^\circ$ and $\vec{V}_a^{-1} = 0.25\angle 0^\circ$. In this SRF-PLL, the control loop bandwidth was high enough to make $v_q \approx 0$, which means that the SRF-PLL was able to instantaneously track the evolution of the unbalanced voltage vector applied to its input. Therefore, the detected phase angle, shown in the second plot of Figure 8.12(c), matches the one calculated by (8.12) and presents oscillations at twice the input frequency. On the other hand, the voltage v_d, shown in the third plot in Figure 8.12(c), matches the value calculated by the expression (8.11) – multiplied by $\sqrt{2}/3$ since the *Park* transformation of (8.20) was rescaled. Consequently, as commented in Section 8.2, the amplitude of

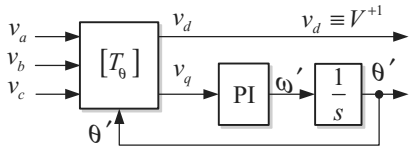

Figure 8.11 Basic block diagram of the SRF-PLL

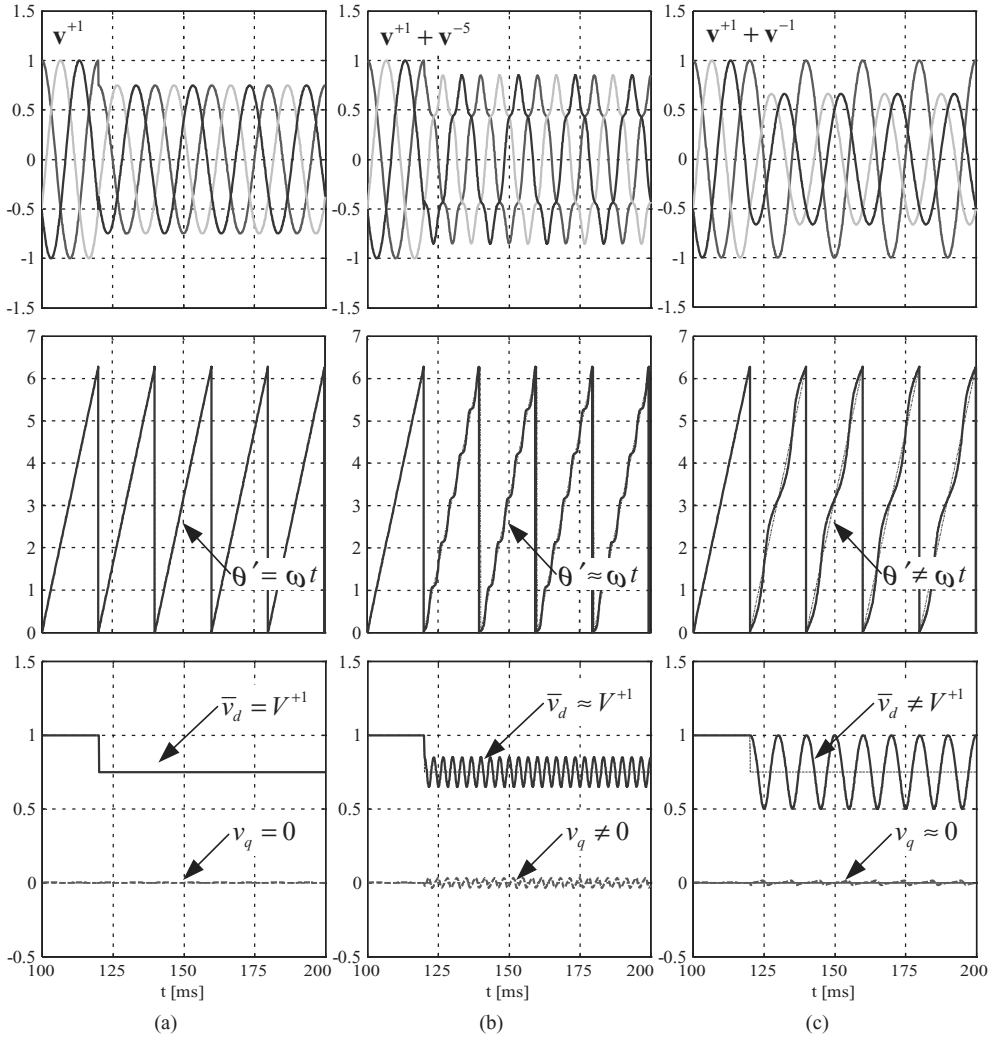

Figure 8.12 Representative waveforms of an SRF-PLL with high bandwidth detecting: (a) a balanced voltage sag, (b) a balanced and distorted voltage sag and (c) an unbalanced voltage sag. From top to bottom, each column shows the three-phase input voltage (p.u.), the detected phase angle (rad) and the detected voltages on the *dq* axis (p.u.)

the positive-sequence component cannot be properly evaluated by just using conventional filtering techniques to extract the average value of v_d.

As previously mentioned, a reduction of the PLL bandwidth can help to attenuate the effect of the distorting components on the SRF-PLL output signals. Figure 8.13 shows some representative plots from an SRF-PLL, tuned with a low bandwidth, when the grid voltage is affected by the same amount of fifth harmonic as in the case of Figure 8.12(b). It can be appreciated in Figure 8.13(c) how the PLL is not able to instantaneously track the angular position of the fifth-order component and thus it gives rise to an oscillating error signal on both axes of the dq reference frame. Therefore, a simple low-pass filter can be used to obtain the average value of the voltage on the d axis, $\bar{v}_d$. Figure 8.13(c) shows the result of applying a second-order low-pass filter with a cut-off frequency of 20 Hz to extract $\bar{v}_d$. It is possible to appreciate in this figure how $\bar{v}_d$ almost perfectly matches the positive-sequence voltage amplitude V^{+1}. Figure 8.13(d) and (e) shows the reconstruction of the detected positive-sequence voltage and its spectrum respectively. These figures confirm that reduction of the PLL bandwidth is an effective measure to obtain high-quality signals at the SRF-PLL output when synchronizing with three-phase voltages polluted by high-order harmonics [14].

However, as evidenced in the following, limitation of the PLL bandwidth is not the most effective solution to extract the positive-sequence component from the unbalanced three-phase voltages resulting from an asymmetrical grid fault.

After applying the rescaled $[T_{\alpha\beta}]$ transformation of (8.21), the unbalanced grid voltage can be expressed on the $\alpha\beta$ reference frame as

$$\boldsymbol{v}_{\alpha\beta} = \begin{bmatrix} v_\alpha \\ v_\beta \end{bmatrix} = V^{+1} \begin{bmatrix} \cos(\omega t) \\ \sin(\omega t) \end{bmatrix} + V^{-1} \begin{bmatrix} \cos(-\omega t) \\ \sin(-\omega t) \end{bmatrix} \tag{8.22}$$

Therefore, if it is assumed that the PLL bandwidth is low enough only to allow tracking the evolution of the positive-sequence component of the input voltage, which means that the dq reference frame rotates at the positive-sequence fundamental frequency, the voltage on the dq axes, resulting from applying the $[T_{dq}]$ transformation of (8.21) on the vector of (8.22), will be given by

$$\boldsymbol{v}_{dq} = V^{+1} \begin{bmatrix} 1 \\ 0 \end{bmatrix} + V^{n} \begin{bmatrix} \cos(-2\omega t) \\ \sin(-2\omega t) \end{bmatrix} \tag{8.23}$$

In (8.23), it has been additionally assumed that the d axis of the SRF perfectly matches the angular position of the positive-sequence component of the input voltage vector. Therefore, (8.23) indicates that the amplitude of the positive-sequence component might be easily obtained by just using any filtering technique to cancel out the oscillation at 2ω present on the d axis signal.

Figure 8.13 allows the performance of the SRF-PLL to be evaluated when a second-order low-pass filter with a cut-off frequency of 20 Hz is used to extract $\bar{v}_d$. Figure 8.13(a) shows the unbalanced input voltage (sag type C with $\vec{V}_a^{+1} = 0.75\angle 0^\circ$, $\vec{V}_a^{-1} = 0.25\angle 0^\circ$). Figure 8.13(b) shows the phase angle detected by the PLL, confirming that the low bandwidth set to the PLL only allows tracking of the positive-sequence component of the unbalanced input voltage vector. Figure 8.13(c) shows in thin lines the voltages on the dq axes of the SRF and in thick

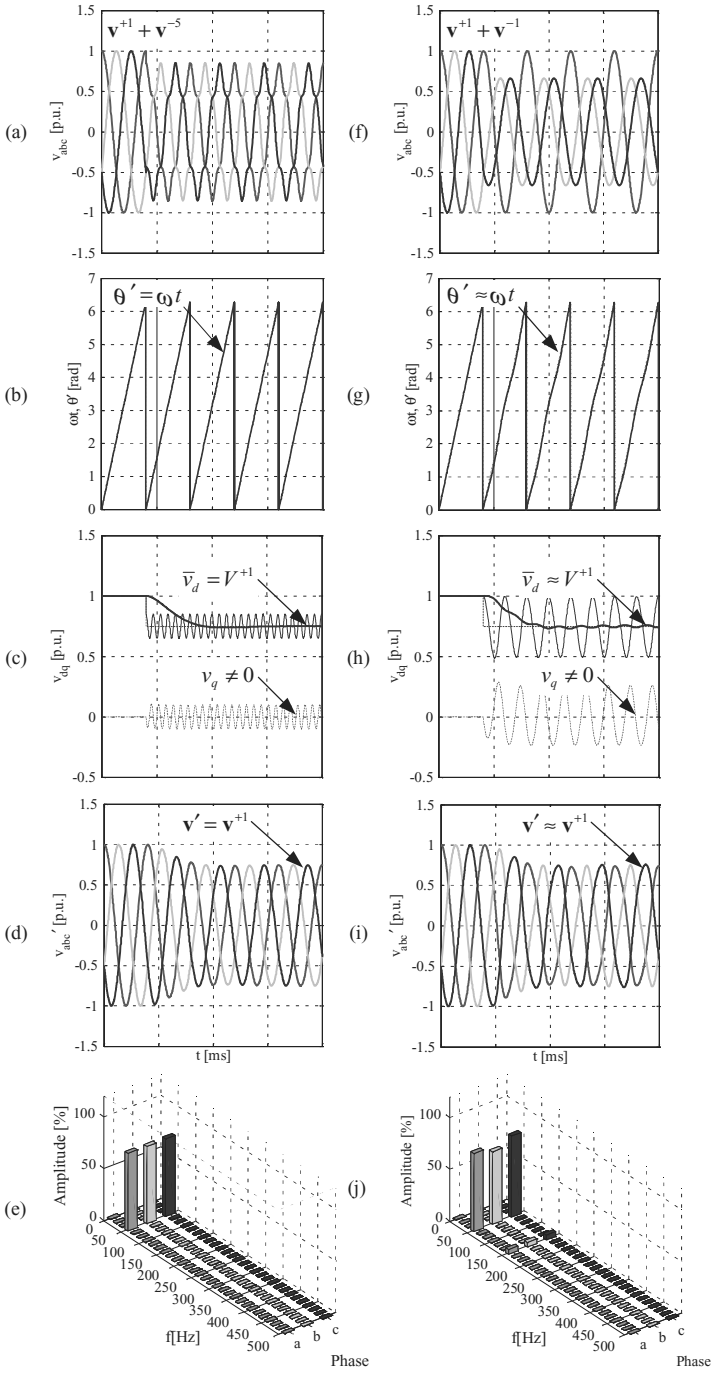

Figure 8.13 Representative waveforms of an SRF-PLL with a low bandwidth: (a, f) three-phase input voltage, (b, g) detected phase angle, (c, h) detected amplitude for the positive-sequence voltage component, (d, i) positive-sequence detected voltage and (e, j) spectrum of the three-phase detected voltage

line the signal $\bar{v}_d$ extracted by the second-order low-pass filter. Using an estimation of the amplitude and phase angle, the positive-sequence voltage waveforms can be reconstructed as shown in Figure 8.13(d). The spectrum of these waveforms is shown in Figure 8.13(e). As appreciated in these last two plots, the detection of the positive-sequence component of the input voltage vector is not accurately detected since the detection of both the amplitude and phase angle is just based on an approximation, i.e. on the attenuation of the oscillation at 2ω generated by the negative-sequence component, and not in the accurate cancellation of such oscillation. Of course, the better the filtering technique applied to cancel out oscillations at 2ω on the dq voltages the better is the synchronization system that will be obtained [15], which is necessary to guarantee that the selected filtering technique presents a frequency adaptive response [16]. The next section of this chapter presents an enhanced synchronization technique based on decoupling the effects of the positive- and negative-sequence components of the input voltage vector.

8.4 The Decoupled Double Synchronous Reference Frame PLL (DDSRF-PLL)

This section presents an improved three-phase synchronous PLL based on using two synchronous reference frames, rotating with positive and negative synchronous speeds,respectively. The usage of this double synchronous reference frame allows decoupling of the effect of the negative-sequence voltage component on the dq signals detected by the synchronous reference frame rotating with positive angular speed, and vice versa, which makes possible accurate grid synchronization even under unbalanced grid faults [17].

8.4.1 The Double Synchronous Reference Frame

Figure 8.14 shows the positive- and negative-sequence components of the unbalanced voltage vector together with a double synchronous reference frame (DSRF) consisting of two rotating reference frames: dq^{+1}, rotating with the positive speed ω' and whose angular position is θ', and dq^{-1}, rotating with the negative speed $-\omega'$ and whose angular position is $-\theta'$.

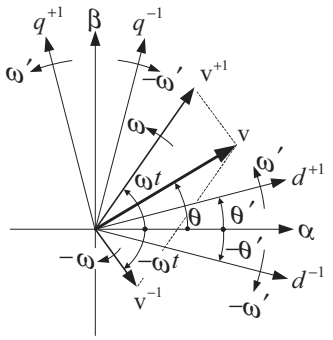

Figure 8.14 Voltage vectors and axes of the DSRF

If it is assumed that the angular position of the positive reference frame dq^{+1} matches the angular position of the positive-sequence voltage vector $\boldsymbol{v}^{+1}$, i.e. if $\theta' = \omega t$, the unbalanced input voltage vector $\boldsymbol{v}$ can be expressed on the DSRF, yielding

$$\boldsymbol{v}_{dq^{+1}} = \begin{bmatrix} v_{d^{+1}} \\ v_{q^{+1}} \end{bmatrix} = \left[T_{dq^{+1}}\right] \cdot \boldsymbol{v}_{\alpha\beta} = V^{+1} \begin{bmatrix} 1 \\ 0 \end{bmatrix} + \boldsymbol{V}^{-1} \begin{bmatrix} \cos(-2\omega t) \\ \sin(-2\omega t) \end{bmatrix} \tag{8.24}$$

$$\boldsymbol{v}_{dq^{-1}} = \begin{bmatrix} v_{d^{-1}} \\ v_{q^{-1}} \end{bmatrix} = \left[T_{dq^{-1}}\right] \cdot \boldsymbol{v}_{\alpha\beta} = V^{+1} \begin{bmatrix} \cos(2\omega t) \\ \sin(2\omega t) \end{bmatrix} + V^{-1} \begin{bmatrix} 1 \\ 0 \end{bmatrix} \tag{8.25}$$

where

$$\left[T_{dq^{+1}}\right] = \left[T_{dq^{-1}}\right]^T = \begin{bmatrix} \cos(\theta') & \sin(\theta') \\ -\sin(\theta') & \cos(\theta') \end{bmatrix} \tag{8.26}$$

Expressions of (8.24) and (8.25) are evidence that the DC values on the dq^{+1} and the dq^{-1} frames correspond to the amplitude of the sinusoidal signals of $\boldsymbol{v}^{+1}$ and $\boldsymbol{v}^{-1}$, while the oscillations at 2ω correspond to the coupling between axes appearing as a consequence of the voltage vectors rotating in opposite directions. Therefore, instead of using any filtering technique for attenuating oscillations at 2ω, a decoupling network is presented in the following to completely cancel out the effect of such oscillations on the synchronous reference frame voltages of the PLL.

8.4.2 The Decoupling Network

To generalize the explanation of the decoupling network used in the DSRF, one supposes a voltage vector consisting of two generic components rotating with $n\omega$ and $m\omega$ frequencies respectively, where n and m can be either positive or negative. Therefore, this generic voltage vector is given by

$$\boldsymbol{v}_{\alpha\beta} = \begin{bmatrix} v_\alpha \\ v_\beta \end{bmatrix} = \boldsymbol{v}^n_{\alpha\beta} + \boldsymbol{v}^m_{\alpha\beta} = V^n \begin{bmatrix} \cos(n\omega t + \phi^n) \\ \sin(n\omega t + \phi^n) \end{bmatrix} + V^m \begin{bmatrix} \cos(m\omega t + \phi^m) \\ \sin(m\omega t + \phi^m) \end{bmatrix} \tag{8.27}$$

Additionally, two rotating reference frames are considered, dq^n and dq^m, whose angular positions are $n\theta'$ and $m\theta'$ respectively, where θ' is the phase angle detected by the PLL. If a perfect synchronization of the PLL is possible, i.e. if $\theta' = \omega t$, with ω the fundamental grid

frequency, the voltage vector in (8.27) can be expressed on the dq^n and dq^m reference frames as follows:

$$\boldsymbol{v}_{dq^n} = \begin{bmatrix} v_{d^n} \\ v_{q^n} \end{bmatrix} = \begin{bmatrix} \overline{v}_{d^n} \\ \overline{v}_{q^n} \end{bmatrix} + \begin{bmatrix} \tilde{v}_{d^n} \\ \tilde{v}_{q^n} \end{bmatrix} = \underbrace{V^n \begin{bmatrix} \cos(\phi^n) \\ \sin(\phi^n) \end{bmatrix}}_{DC\ terms}$$
$$+ \underbrace{V^m \cos(\phi^m) \begin{bmatrix} \cos((n-m)\omega t) \\ -\sin((n-m)\omega t) \end{bmatrix} + V^m \sin(\phi^m) \begin{bmatrix} \sin((n-m)\omega t) \\ \cos((n-m)\omega t) \end{bmatrix}}_{AC\ terms} \quad (8.28)$$

$$\boldsymbol{v}_{dq^m} = \begin{bmatrix} v_{d^m} \\ v_{q^m} \end{bmatrix} = \begin{bmatrix} \overline{v}_{d^m} \\ \overline{v}_{q^m} \end{bmatrix} + \begin{bmatrix} \tilde{v}_{d^m} \\ \tilde{v}_{q^m} \end{bmatrix} = \underbrace{V^m \begin{bmatrix} \cos(\phi^m) \\ \sin(\phi^m) \end{bmatrix}}_{DC\ terms}$$
$$+ \underbrace{V^n \cos(\phi^n) \begin{bmatrix} \cos((n-m)\omega t) \\ \sin((n-m)\omega t) \end{bmatrix} + V^n \sin(\phi^n) \begin{bmatrix} -\sin((n-m)\omega t) \\ \cos((n-m)\omega t) \end{bmatrix}}_{AC\ terms} \quad (8.29)$$

As shown by (8.28) and (8.29), the amplitude of the AC terms in the dp^n axes depends on the DC terms of the signals on the dq^m axes, and vice versa. Therefore, once the coupling terms between both reference frames are identified, a decoupling cell, such as the one shown in Figure 8.15, can be designed to cancel out the oscillations generated by the voltage vector $\boldsymbol{v}^m$ on the dq^n axes signals. To cancel out the oscillations in the dq^m axes signals, the same structure may be used, but with swapping of the m and n indexes in it. In Figure 8.15, the DC terms on the dq^m axes are represented as $\bar{v}_{d^m}$ and $\bar{v}_{q^m}$. As shown in Figure 8.16, a

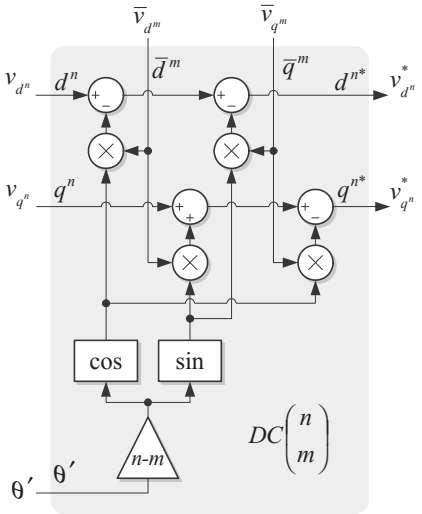

Figure 8.15 Decoupling cell for cancelling the effect of $\boldsymbol{v}^m$ on the dq^n frame signals

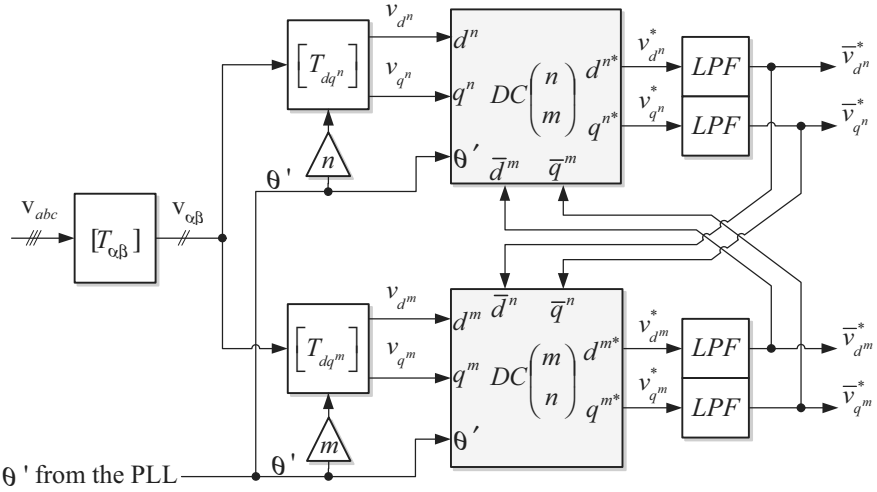

Figure 8.16 Decoupled double synchronous reference frame (DDSRF)

cross-feedback decoupling network is used to estimate the value of these DC terms on the positive and negative reference frames. In this decoupling network, the estimated DC terms are named as $\overline{v}^*_{d^m}$, $\overline{v}^*_{q^m}$, $\overline{v}^*_{d^n}$ and $\overline{v}^*_{q^n}$ and the LPF block is a low-pass filter such as

$$LPF(s) = \frac{\omega_f}{s + \omega_f} \tag{8.30}$$

The decoupled double synchronous reference frame (DDSRF) of Figure 8.16 allows free-oscillation signals to be obtained on the dq^m and dq^n reference frames. By setting $n = +1$ and $m = -1$, this network decouples information about the positive- and negative-sequence components of either voltage or current in unbalanced three-phase systems, which makes it a useful tool for synchronous controllers during unbalanced grid faults. This network can be also used to decouple other frequency/sequence components simply by setting the proper values for the m and n coefficients.

8.4.3 Analysis of the DDSRF

The state-space model of the DDSRF and some relevant expressions showing its performance have already been presented in reference [17], so this section will present a more intuitive analysis on the complex-frequency domain to improve understanding about the DDSRF performance during unbalanced grid faults. From (8.27), the unbalanced voltage during a grid fault, consisting of positive- and negative-sequence components at the fundamental frequency, can be generically described as

$$\boldsymbol{v}_{\alpha\beta} = \begin{bmatrix} v_\alpha \\ v_\beta \end{bmatrix} = \boldsymbol{v}^{+1}_{\alpha\beta} + \boldsymbol{v}^{-1}_{\alpha\beta} = V^{+1}\begin{bmatrix} \cos(\omega t + \phi^{+1}) \\ \sin(\omega t + \phi^{+1}) \end{bmatrix} + V^{-1}\begin{bmatrix} \cos(-\omega t + \phi^{-1}) \\ \sin(-\omega t + \phi^{-1}) \end{bmatrix} \tag{8.31}$$

The projection of this voltage vector on the dq^{+1} and dq^{-1} reference frames can be easily obtained simply by setting $n = +1$ and $m = -1$ in (8.28) and (8.29). After rearranging equations, the dq signals on the positive and negative reference frames are given by

$$\boldsymbol{v}_{dq^{+1}} = \begin{bmatrix} v_{d^{+1}} \\ v_{q^{+1}} \end{bmatrix} = V^{+1} \begin{bmatrix} \cos(\phi^{+1}) \\ \sin(\phi^{+1}) \end{bmatrix} + V^{-1} \begin{bmatrix} \cos(2\omega t) & \sin(2\omega t) \\ -\sin(2\omega t) & \cos(2\omega t) \end{bmatrix} \begin{bmatrix} \cos(\phi^{-1}) \\ \sin(\phi^{-1}) \end{bmatrix} \tag{8.32}$$

$$\boldsymbol{v}_{dq^{-1}} = \begin{bmatrix} v_{d^{-1}} \\ v_{q^{-1}} \end{bmatrix} = V^{-1} \begin{bmatrix} \cos(\phi^{-1}) \\ \sin(\phi^{-1}) \end{bmatrix} + V^{+1} \begin{bmatrix} \cos(2\omega t) & -\sin(2\omega t) \\ \sin(2\omega t) & \cos(2\omega t) \end{bmatrix} \begin{bmatrix} \cos(\phi^{+1}) \\ \sin(\phi^{+1}) \end{bmatrix} \tag{8.33}$$

These expressions clearly give evidence that the AC terms in the dq^{+1} axes result from the DC terms in the dq^{-1} axes being affected by a rotating transformation matrix at 2ω frequency. A similar conclusion can be obtained for AC signals on the dq^{-1} reference frame. These rotating transformation matrices are given by

$$\left[T_{dq^{+2}}\right] = \left[T_{dq^{-2}}\right]^{\mathrm{T}} = \begin{bmatrix} \cos(2\omega t) & \sin(2\omega t) \\ -\sin(2\omega t) & \cos(2\omega t) \end{bmatrix} \tag{8.34}$$

Therefore, (8.32) and (8.33) can be rewritten as

$$\boldsymbol{v}_{dq^{+1}} = \begin{bmatrix} v_{d^{+1}} \\ v_{q^{+1}} \end{bmatrix} = \overline{\boldsymbol{v}}_{dq^{+1}} + \left[T_{dq^{+2}}\right] \overline{\boldsymbol{v}}_{dq^{-1}} \tag{8.35}$$

$$\boldsymbol{v}_{dq^{-1}} = \begin{bmatrix} v_{d^{-1}} \\ v_{q^{-1}} \end{bmatrix} = \overline{\boldsymbol{v}}_{dq^{-1}} + \left[T_{dq^{-2}}\right] \overline{\boldsymbol{v}}_{dq^{+1}} \tag{8.36}$$

where

$$\overline{\boldsymbol{v}}_{dq^{+1}} = \begin{bmatrix} \overline{v}_{d^{+1}} \\ \overline{\boldsymbol{v}}_{q^{+1}} \end{bmatrix} = V^{+1} \begin{bmatrix} \cos(\phi^{+1}) \\ \sin(\phi^{+1}) \end{bmatrix} \quad \text{and} \quad \overline{\boldsymbol{v}}_{dq^{-1}} = \begin{bmatrix} \overline{v}_{d^{-1}} \\ \overline{v}_{q^{-1}} \end{bmatrix} = V^{-1} \begin{bmatrix} \cos(\phi^{-1}) \\ \sin(\phi^{-1}) \end{bmatrix}$$

represent the amplitude of sequence components applied to the input of the DDSRF. Thus, (8.35) and (8.36) give evidence that the relationship between the signals on the positive and negative reference frames are given by

$$\boldsymbol{v}_{dq^{+1}} = \left[T_{dq^{+2}}\right] \boldsymbol{v}_{dq^{-1}} \quad \text{and} \quad \boldsymbol{v}_{dq^{-1}} = \left[T_{dq^{-2}}\right] \boldsymbol{v}_{dq^{+1}} \tag{8.37}$$

As a result, the estimated values at the output of the DDSRF can be written as:

$$\overline{\boldsymbol{v}}^{*}_{dq^{+1}} = \begin{bmatrix} \overline{v}^{*}_{d^{+1}} \\ \overline{v}^{*}_{q^{+1}} \end{bmatrix} = [F] \left\{ \boldsymbol{v}_{dq^{+1}} - \left[T_{dq^{+2}}\right] \overline{\boldsymbol{v}}^{*}_{dq^{-1}} \right\} \tag{8.38}$$

$$\overline{\boldsymbol{v}}^{*}_{dq^{-1}} = \begin{bmatrix} \overline{v}^{*}_{d^{-1}} \\ \overline{v}^{*}_{q^{-1}} \end{bmatrix} = [F] \left\{ \boldsymbol{v}_{dq^{-1}} - \left[T_{dq^{-2}}\right] \overline{\boldsymbol{v}}^{*}_{dq^{+1}} \right\} \tag{8.39}$$

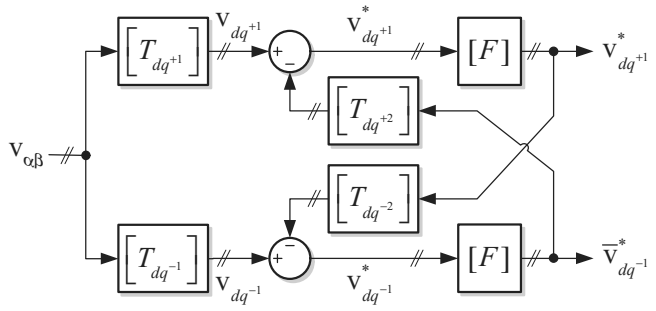

Figure 8.17 Block diagram of the DDSRF with n = +1 and m = −1

where

$$[F] = \begin{bmatrix} LPF(s) & 0 \\ 0 & LPF(s) \end{bmatrix}$$

Therefore, the DDSRF of Figure 8.16 can be represented for the particular case of the positive- and negative-sequence components at the fundamental frequency, as Figure 8.17 shows.

In order not to extend excessively the analysis of the DDSRF, only an estimation of the positive-sequence component will be considered in the following. Therefore, substituting (8.39) in (8.38) we obtain

$$\overline{\boldsymbol{v}}^{*}_{dq^{+1}} = [F]\left\{\boldsymbol{v}_{dq^{+1}} - \left[T_{dq^{+2}}\right][F]\left(\boldsymbol{v}_{dq^{-1}} - \left[T_{dq^{-2}}\right]\overline{\boldsymbol{v}}^{*}_{dq^{+1}}\right)\right\} \tag{8.40}$$

and using the relationships of (8.37), we arrive at

$$\overline{\boldsymbol{v}}^{*}_{dq^{+1}} = [F]\left\{\boldsymbol{v}_{dq^{+1}} - \left[T_{dq^{+2}}\right][F]\left(\left[T_{dq^{-2}}\right]\boldsymbol{v}_{dq^{+1}} - \left[T_{dq^{-2}}\right]\overline{\boldsymbol{v}}^{*}_{dq^{+1}}\right)\right\} \tag{8.41}$$

$$\overline{\boldsymbol{v}}^{*}_{dq^{+1}} = [F]\left\{\boldsymbol{v}_{dq^{+1}} - \left[T_{dq^{+2}}\right][F]\left[T_{dq^{-2}}\right]\left(\boldsymbol{v}_{dq^{+1}} - \overline{\boldsymbol{v}}^{*}_{dq^{+1}}\right)\right\} \tag{8.42}$$

A very amusing academic exercise is to determine the matrix resulting from $\left[T_{dq^{+2}}\right][F]\left[T_{dq^{-2}}\right]$. Some useful directions regarding how these matrices should be operated can be found in references [18] and [19]. As a result of such operations it can be concluded that

$$\begin{aligned}[F_{-2}] &= \left[T_{dq^{+2}}\right][F]\left[T_{dq^{-2}}\right] \\ &= \frac{1}{2}\begin{bmatrix} (LPF(s+\mathrm{j}2\omega) + LPF(s-\mathrm{j}2\omega)) & \mathrm{j}\,(-LPF(s+\mathrm{j}2\omega) + LPF(s-\mathrm{j}2\omega)) \\ \mathrm{j}\,(LPF(s+\mathrm{j}2\omega) - LPF(s-\mathrm{j}2\omega)) & (LPF(s+\mathrm{j}2\omega) + LPF(s-\mathrm{j}2\omega)) \end{bmatrix}\end{aligned}$$

$$[F_{-2}] = [F_{+2}]^{\mathrm{T}} = \frac{1}{2}\begin{bmatrix} \dfrac{\omega_f\left(s+\omega_f\right)}{s^2+2s\omega_f+\omega_f^2+(2\omega)^2} & -\dfrac{\omega_f\omega}{s^2+2s\omega_f+\omega_f^2+(2\omega)^2} \\ \dfrac{\omega_f\omega}{s^2+2s\omega_f+\omega_f^2+(2\omega)^2} & \dfrac{\omega_f\,(s+\omega_F)}{s^2+2s\omega_f+\omega_f^2+(2\omega)^2} \end{bmatrix} \tag{8.43}$$

Therefore, (8.42) can be simplified as

$$\overline{\boldsymbol{v}}^{*}_{dq^{+1}} = [F]\left\{\boldsymbol{v}_{dq^{+1}} - [F_{-2}]\left(\boldsymbol{v}_{dq^{+1}} - \overline{\boldsymbol{v}}^{*}_{dq^{+1}}\right)\right\} \tag{8.44}$$

and regrouping terms yields

$$\{[I] - [F][F_{-2}]\}\,\overline{\boldsymbol{v}}^{*}_{dq^{+1}} = [F]\,\{[I] - [F_{-2}]\}\,\boldsymbol{v}_{dq^{+1}} \tag{8.45}$$

where $[I]$ is the identity matrix. As a result, the following expression describes the relationship between the signals on the positive-sequence frame and the estimated value for the positive-sequence component at the output of the DDSRF:

$$\overline{\boldsymbol{v}}^{*}_{dq^{+1}} = \{[I] - [F][F_{-2}]\}^{-1}\,[F]\,\{[I] - [F_{-2}]\}\,\boldsymbol{v}_{dq^{+1}} \tag{8.46}$$

After operating, this relationship is given by

$$\frac{\overline{\boldsymbol{v}}^{*}_{dq^{+1}}}{\boldsymbol{v}_{dq^{+1}}} = \begin{bmatrix} H_{11} & H_{12} \\ H_{21} & H_{22} \end{bmatrix}\;;\;\begin{cases} H_{11} = H_{22} = H\left(s^3 + 2\omega_f s^2 + 4\omega^2 s + 4\omega_f\omega^2\right) \\ H_{12} = -H_{21} = -H\left(2\omega_f\omega s\right) \end{cases} \tag{8.47}$$

where

$$H = \frac{\omega_f}{s^4 + 4\omega_f s^3 + 4\left(\omega_f^2 + \omega^2\right)s^2 + 8\omega_f\omega^2 s + 4\omega_f^2\omega^2} \tag{8.48}$$

The transfer function for the negative-sequence output of the DDSRF is given simply by transposing the matrix shown in (8.47), and is obtained by following the same steps as in the positive-sequence case.

The DDSRF is a very useful tool when dealing with three-phase systems, since it is a sequence separator that allows independent control of the positive- and negative-sequence components of voltage and/or current during unbalanced grid faults. For this reason, the transfer functions shown in (8.47) are very important for correct implementation of the low-voltage ride-through capability in power converters under unbalanced grid fault conditions.

In the transfer functions of (8.47), it is supposed that the frequency ω is given by a PLL and matches the fundamental frequency of the grid, while the cut-off frequency of the low-pass filer, ω_f, is properly set in design time to obtain the required performance of the system. Figure 8.18 shows the evolution of the signal on the d^{+1} axis of the positive-sequence reference frame of the DDSRF, $\overline{v}^{*}_{d^{+1}}$, when $\boldsymbol{v}_{dq^{+1}}$ is suddenly applied to its input in the form of a unitary step for different values of ω_f. From this figure, it can be concluded that a reasonable trade-off between the time response and oscillation damping can be achieved by setting $\omega_f = \omega/\sqrt{2}$ rad/s [17].

8.4.4 Structure and Response of the DDSRF-PLL

The block diagram of the DDSRF-PLL is shown in Figure 8.19. As shown in the figure, this PLL is an extension of the conventional three-phase SRF-PLL structure. In this PLL, in order to

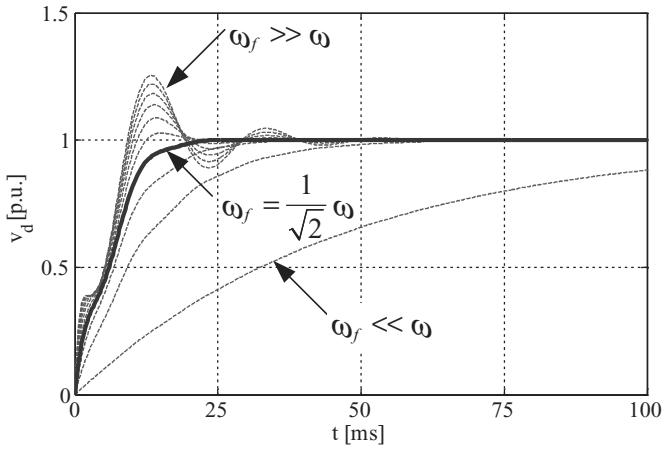

Figure 8.18 Step response of the signal $\overline{v}^*_{d^{+1}}$ at the output of the DDSRF

obtain a similar dynamic response for different grid voltage amplitudes, the phase-angle error signal $v_q{}^{+1}$ is adaptively normalized to the amplitude of the positive-sequence input vector. Moreover, the rated grid frequency is added as a feed-forward parameter, ω_{ff}, to accelerate the pulling process of the PLL. However, the most significant performance improvement in this PLL comes from the decoupling network added to the DSRF.

The decoupling network of the DDSRF-PLL completely cancels out the oscillations at 2ω on the dq^{+1} and dq^{-1} reference frame signals. Therefore, there is no need to reduce the bandwidth of the PLL to attenuate such oscillations and the real amplitude of the unbalanced input voltage sequence components are indeed exactly detected.

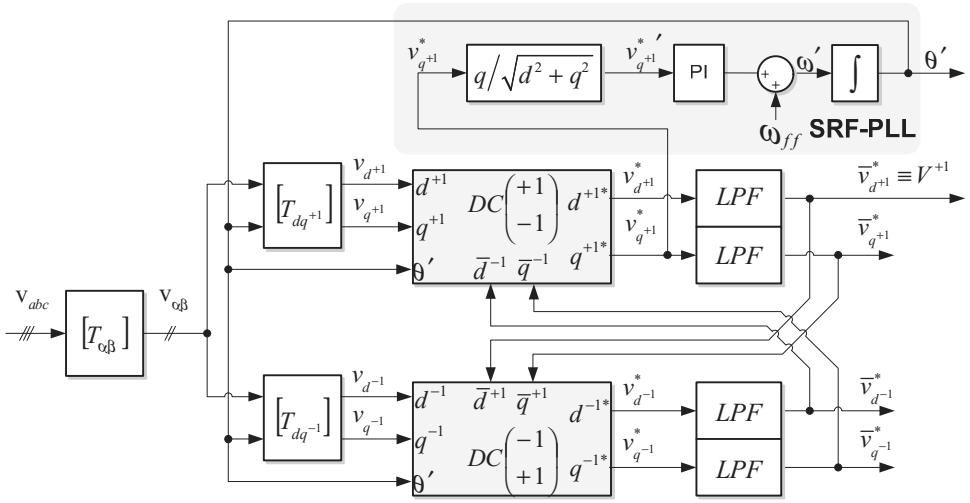

Figure 8.19 Structure of the DDSRF-PLL

Figure 8.20 shows the response of the DDSRF-PLL when used in the estimation of the sequence components of the grid voltage during a sag type C with $\vec{V}_a^{+1} = 0.5\angle -30^\circ$ and $\vec{V}_a^{-1} = 0.25\angle +60^\circ$. In this study case, the fundamental grid frequency is $\omega = 314.1$ rad/s. Therefore, the cut-off frequency of the low-pass filter was set to $\omega_f = \omega/\sqrt{2} = 222.1$ rad/s and the parameters of the PI controller were set to $k_p = 222.1$ and $k_i = 9 \times 10^{-3}$, which results in a settling time around 40 ms according to the guidelines given in [20] and in Section 4.2.2 of Chapter 4.

The plot of Figure 8.20(a) shows the three-phase unbalanced voltages, which experience a jump in the phase angle, as evidenced by the vector locus shown in Figure 8.20(b). The actual and the detected phase angle are plotted in Figure 8.20(c). This figure shows how the PLL is able to lock the phase-angle jump after a transient period, which roughly matches the settling time of the PLL calculated by the expression (4.37) in Chapter 4. This settling time, approximately 40 ms, can be clearly observed in Figure 8.20(d), which represents the frequency detected by the DDSRF-PLL. From this figure, it is worth highlighting the fact that the large amplitude of the transient oscillation in the detected frequency as a consequence of the phase-angle jump occurred in the grid voltage. The existence of such significant oscillations in the detected frequency, which is indeed one of the most stable magnitudes in power systems, can be considered as a drawback of the DDSRF-PLL in certain applications. Figure 8.20(e) shows the dq^{+1} signals on the axes of the positive reference frame (thin traces) and the resultant signals at the output of the DDSRF (thick traces). Likewise, the dq^{-1} signals on the negative-sequence reference frame are shown Figure 8.20(f). In this last figure, the d^{-1} component is equal to zero because of a geometrical coincidence. Since the PLL is controlling the position of the dq^{+1} reference frame, only the q^{+1} signal at the output of the DDSRF is forced to be equal to zero. Both d^{-1} and q^{-1} signals at the output of the DDSRF can take any arbitrary value depending on the relative angular position between the positive- and negative-sequence voltage vectors. Figure 8.20(e) and (f) shows how the DDSRF perfectly decouples the positive- and negative-sequence voltage components and obtains free oscillation signals describing the amplitude of the positive- and negative-sequence voltage vectors applied to its input. From the detected phase angle and amplitudes, the positive- and negative-sequence three-phase voltages can be readily reconstructed as shown in Figure 8.20(g) and (h).

The DDSRF-PLL is an effective synchronization solution for the implementation of synchronous controllers for three-phase power converters, mainly if they provide low-voltage ride-through capabilities under unbalanced grid faults. However, as presented in Chapter 9, the power converter controllers can also be implemented on the stationary reference frame by using resonant controllers. In such a case, the grid voltage phase angle is not the most important synchronization variable – the grid frequency is. Since the grid frequency is a more stable variable than the grid phase angle, it is intuitive to think that controllers based on grid frequency detection will present a more robust performance than those based on phase-angle detection during grid faults. In the next section, a synchronization system based on adaptive filters working on the stationary reference frame is presented as a suitable technique to be applied in the implementation of resonant controllers for three-phase converters.

8.5 The Double Second-Order Generalized Integrator FLL (DSOGI-FLL)

The DSOGI-FLL exploits the instantaneous symmetrical components method by using adaptive filters based on the second-order generalized integrator [21, 22]. As previously presented

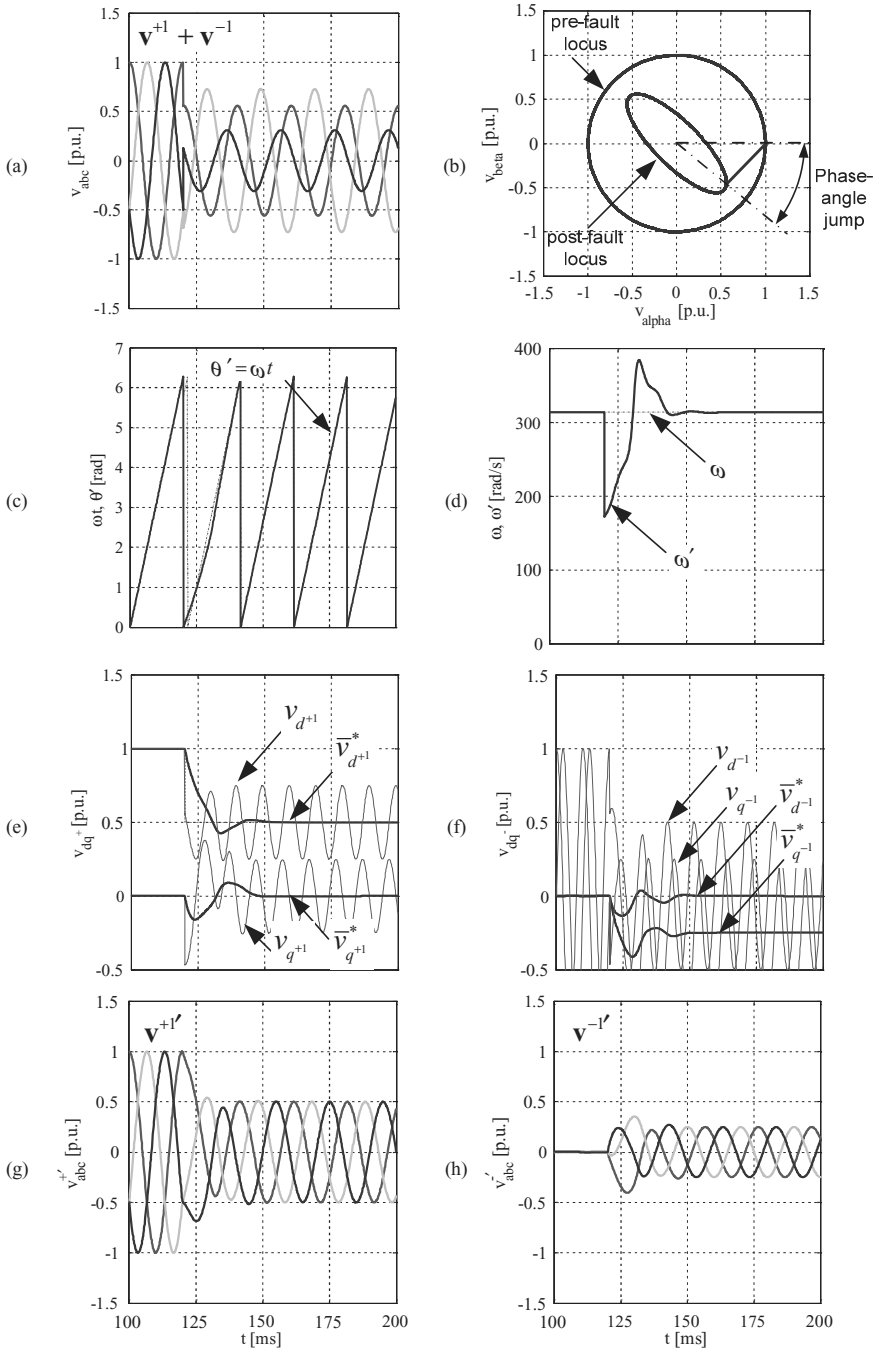

Figure 8.20 Representative waveforms of a DDSRF-PLL: (a) three-phase input voltage, (b) voltage vector locus, (c) detected phase angle, (d) detected frequency, (e) detected *dq* signals for the positive-sequence component, (f) detected *dq* signals for the negative-sequence component, (g) detected positive-sequence three-phase voltages and (h) detected negative-sequence three-phase voltages

in this chapter, an unbalanced three-phase system can be systematically analysed by transforming its unbalanced phasors into a set of symmetrical components according to the *Fortescue* transformation matrix shown in (8.14) [23]. The symmetrical components method can also be applied in the time domain analysis by using the *Lyon* transformation [24]. According to this method, a voltage vector $\boldsymbol{v}_{abc}$ consisting of three unbalanced sinusoidal waveforms can be split up into its instantaneous positive-, negative- and zero-sequence components, $\boldsymbol{v}_{abc} = \boldsymbol{v}^{+}_{abc} + \boldsymbol{v}^{-}_{abc} + \boldsymbol{v}^{0}_{abc}$, by applying the following transformations:

$$\boldsymbol{v}^{+}_{abc} = [T_{+}]\ \boldsymbol{v}_{abc};\quad \begin{bmatrix} v^{+}_{a} \\ v^{+}_{b} \\ v^{+}_{c} \end{bmatrix} = \frac{1}{3}\begin{bmatrix} 1 & a & a^2 \\ a^2 & 1 & a \\ a & a^2 & 1 \end{bmatrix}\begin{bmatrix} v_a \\ v_b \\ v_c \end{bmatrix} \tag{8.49}$$

$$\boldsymbol{v}^{-}_{abc} = [T_{-}]\ \boldsymbol{v}_{abc};\quad \begin{bmatrix} v^{-}_{a} \\ v^{-}_{b} \\ v^{-}_{c} \end{bmatrix} = \frac{1}{3}\begin{bmatrix} 1 & a^2 & a \\ a & 1 & a^2 \\ a^2 & a & 1 \end{bmatrix}\begin{bmatrix} v_a \\ v_b \\ v_c \end{bmatrix} \tag{8.50}$$

$$\boldsymbol{v}^{0}_{abc} = [T_{0}]\ \boldsymbol{v}_{abc};\quad \begin{bmatrix} v^{0}_{a} \\ v^{0}_{b} \\ v^{0}_{c} \end{bmatrix} = \frac{1}{3}\begin{bmatrix} 1 & 1 & 1 \\ 1 & 1 & 1 \\ 1 & 1 & 1 \end{bmatrix}\begin{bmatrix} v_a \\ v_b \\ v_c \end{bmatrix} \tag{8.51}$$

where a is a particular version of the *Fortescue* operator and represents a kind of time-shifting over the instantaneous sinusoidal input signals at the fundamental grid frequency, equivalent to a 120° phase-shifting.

In three-phase three-wire grid-connected power converters, the main interest lies in controlling the positive- and negative-sequence components of the injected current. In turn, the grid synchronization system should be focused on perfectly tracking the positive- and negative-sequence components of the grid voltage at the point of common coupling.

The sequence components of $\boldsymbol{v}_{abc}$ can be expressed on the $\alpha\beta$ reference frame by using either the transformation matrix of (8.5) or its rescaled version of (8.21), yielding

$$\begin{aligned} \boldsymbol{v}^{+}_{\alpha\beta} &= \left[T_{\alpha\beta}\right]\ \boldsymbol{v}^{+}_{abc} \\ \boldsymbol{v}^{-}_{\alpha\beta} &= \left[T_{\alpha\beta}\right]\ \boldsymbol{v}^{-}_{abc} \end{aligned} \tag{8.52}$$

Substituting (8.49) and (8.50) we obtain

$$\begin{aligned} \boldsymbol{v}^{+}_{\alpha\beta} &= \left[T_{\alpha\beta}\right]\ [T_{+}]\ \boldsymbol{v}_{abc} \\ \boldsymbol{v}^{-}_{\alpha\beta} &= \left[T_{\alpha\beta}\right]\ [T_{-}]\ \boldsymbol{v}_{abc} \end{aligned} \tag{8.53}$$

and applying the inverse transformation $\left[T_{\alpha\beta}\right]^{-1}$ we have

$$\begin{aligned} \boldsymbol{v}^{+}_{\alpha\beta} &= \left[T_{\alpha\beta}\right]\ [T_{+}]\ \left[T_{\alpha\beta}\right]^{-1}\ \boldsymbol{v}_{\alpha\beta} \\ \boldsymbol{v}^{-}_{\alpha\beta} &= \left[T_{\alpha\beta}\right]\ [T_{-}]\ \left[T_{\alpha\beta}\right]^{-1}\ \boldsymbol{v}_{\alpha\beta} \end{aligned} \tag{8.54}$$

Finally, after operating these transformation matrixes we arrive at the following expressions:

$$\boldsymbol{v}^{+}_{\alpha\beta} = \left[T_{\alpha\beta^{+}}\right]\boldsymbol{v}_{\alpha\beta}; \quad \left[T_{\alpha\beta^{+}}\right] = \frac{1}{2}\begin{bmatrix} 1 & -q \\ q & 1 \end{bmatrix} \tag{8.55}$$

$$\boldsymbol{v}^{-}_{\alpha\beta} = \left[T_{\alpha\beta^{-}}\right]\boldsymbol{v}_{\alpha\beta}; \quad \left[T_{\alpha\beta^{-}}\right] = \frac{1}{2}\begin{bmatrix} 1 & q \\ -q & 1 \end{bmatrix} \tag{8.56}$$

where $q = \mathrm{e}^{-\mathrm{j}\pi/2}$ is a 90°-lagging phase-shifting operator applied on the time domain to obtain an in-quadrature version of the input waveforms.

8.5.1 Structure of the DSOGI

Different techniques to implement a quadrature signal generator (QSG) were presented in Chapter 4. In the DSOGI, the operator q of (8.55) and (8.56) is implemented by using the second-order AF based on a SOGI (SOGI-QSG), which was presented in Section 4.5.3 of Chapter 4 as an effective method to obtain a set of two in-quadrature output signals from a given sinusoidal input signal. Moreover, the filtering characteristic of the SOGI-QSG attenuates the effect of the distorting high-order harmonics from the input to the output.

The structure of the DSOGI is presented in Figure 8.21. As observed in this figure, two SOGI-QSGs are in charge of generating the direct and in-quadrature signals for the α and β components of the input vector, i.e. v'_α, v'_β, qv'_α and qv'_β respectively. These signals are

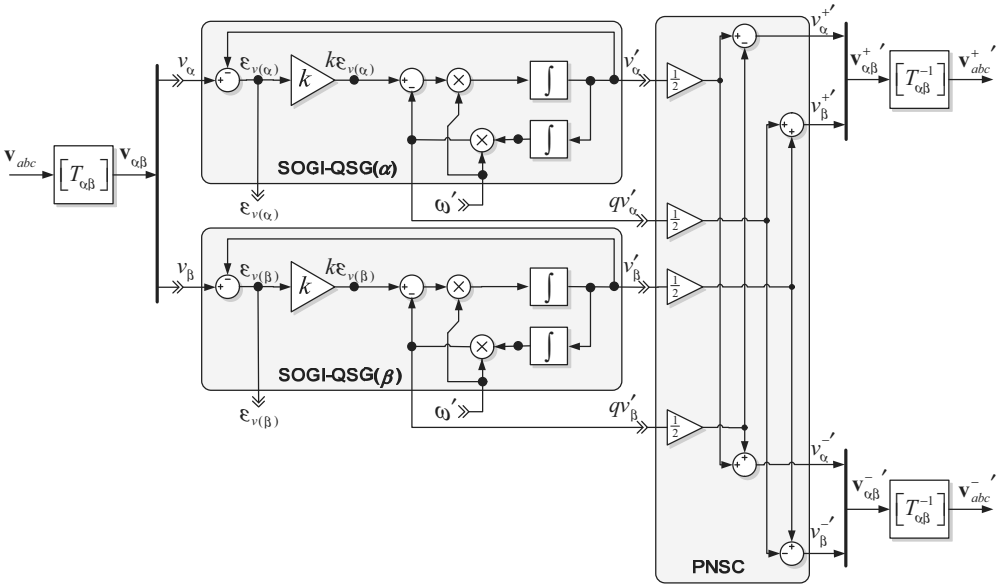

Figure 8.21 Structure of the DSOGI

provided as inputs to a positive-/negative-sequence calculation block (PNSC), which computes the sequence components on the $\alpha\beta$ reference frame according to (8.55) and (8.56).

8.5.2 Relationship between the DSOGI and the DDSRF

According to (8.55), the transfer function from the unbalance input voltage vector to the positive-sequence component detected by the DSOGI is given by

$$\boldsymbol{v}_{\alpha\beta}^{+} = \left[T_{\alpha\beta^{+}}\right] \boldsymbol{v}_{\alpha\beta} = \frac{1}{2}\begin{bmatrix} D(s) & -Q(s) \\ Q(s) & D(s) \end{bmatrix} \boldsymbol{v}_{\alpha\beta} = \frac{1}{2}\frac{k\omega'}{s^2 + k\omega' s + \omega'^2}\begin{bmatrix} s & -\omega' \\ \omega' & s \end{bmatrix} \boldsymbol{v}_{\alpha\beta} \tag{8.57}$$

where $D(s)$ and $Q(s)$ are the characteristic transfer functions of the SOGI-QSG and were already presented in Section 4.5.3 of Chapter 4. The negative-sequence component at the output of the DSOGI can be calculated by simply transposing the matrix of (8.57).

The DDSRF was analysed in Section 8.4.3 and its transfer function on the synchronous reference frame was presented in (8.47). To translate the transfer function of the DDSRF from the synchronous reference frame to the stationary one it is necessary to operate the following transformation:

$$\boldsymbol{v}_{\alpha\beta}^{+} = \left[T_{dq^{+}}\right] \begin{bmatrix} H_{11} & H_{12} \\ H_{21} & H_{22} \end{bmatrix} \left[T_{dq^{+}}\right]^{-1} \boldsymbol{v}_{\alpha\beta} \tag{8.58}$$

Taking into account that $H_{11} = H_{22}$ and $H_{12} = -H_{21}$, we arrive at

$$\boldsymbol{v}_{\alpha\beta}^{+} = \frac{1}{2}\begin{bmatrix} H_a - \mathrm{j}H_b & \mathrm{j}H_c + H_d \\ -\mathrm{j}H_c - H_d & H_a - \mathrm{j}H_b \end{bmatrix} \boldsymbol{v}_{\alpha\beta} \tag{8.59}$$

where

$$\begin{aligned} H_a &= \left(H_{11}\left(s + \mathrm{j}\omega'\right) + H_{11}\left(s - \mathrm{j}\omega'\right)\right) \\ H_b &= \left(H_{12}\left(s + \mathrm{j}\omega'\right) - H_{12}\left(s - \mathrm{j}\omega'\right)\right) \\ H_c &= \left(H_{11}\left(s + \mathrm{j}\omega'\right) - H_{11}\left(s - \mathrm{j}\omega'\right)\right) \\ H_d &= \left(H_{12}\left(s + \mathrm{j}\omega'\right) + H_{12}\left(s - \mathrm{j}\omega'\right)\right) \end{aligned} \tag{8.60}$$

Expanding and regrouping (8.59), the following transfer functions are obtained to describe the performance of the DDSRF on the stationary $\alpha\beta$ reference frame:

$$\boldsymbol{v}_{\alpha\beta}^{+} = \frac{\omega_f}{s^2 + 2\omega_f s + \omega'^2}\begin{bmatrix} s & -\omega' \\ \omega' & s \end{bmatrix} \boldsymbol{v}_{\alpha\beta} \tag{8.61}$$

where ω_f is the cuf-off frequency of the first-order low-pass filter and ω' is the frequency detected by the PLL.

Expressions (8.57) and (8.61) show that the DSOGI and the DDSRF are two equivalent systems, which perform the same function – sequence separation – on two different reference

frames. In principle, the DSOGI and the DDSRF would have the same dynamic response when $k = 2\omega_f/\omega'$ in (8.57). However, it is worth remarking that the DSOGI performance depends on the frequency detected by the FLL, while the DDSRF depends on the phase angle detected by the PLL. Therefore, the response of the DSOGI-FLL and the DDSRF-PLL will not exactly be equal in practice since the FLL and the PLL are two completely different systems with a different dynamic response.

To analyse the frequency response of the DSOGI, the expression of (8.57) can be written in the frequency domain ($s = \mathrm{j}\omega$) as follows:

$$\begin{bmatrix} v_\alpha^+ \\ v_\beta^+ \end{bmatrix} = \frac{1}{2}\begin{bmatrix} D(\mathrm{j}\omega) & -Q(\mathrm{j}\omega) \\ Q(\mathrm{j}\omega) & D(\mathrm{j}\omega) \end{bmatrix}\begin{bmatrix} \boldsymbol{v}_\alpha \\ \boldsymbol{v}_\beta \end{bmatrix} = \frac{1}{2}\frac{k\omega'}{\left(\omega'^2 - \omega^2\right) + \mathrm{j}k\omega'\omega}\begin{bmatrix} \mathrm{j}\omega & -\omega' \\ -\omega & \mathrm{j}\omega \end{bmatrix}\begin{bmatrix} v_\alpha \\ v_\beta \end{bmatrix} \tag{8.62}$$

Considering that the $\alpha\beta$ components of a balanced positive-sequence voltage vector at frequency ω keep the following steady-state relationship on the frequency domain:

$$\boldsymbol{v}_\beta(\mathrm{j}\omega) = -\mathrm{j}v_\alpha(\mathrm{j}\omega) \tag{8.63}$$

Therefore, the steady-state transfer function of the DSOGI on the frequency domain can be written as

$$\begin{bmatrix} v_\alpha^+ \\ v_\beta^+ \end{bmatrix} = \frac{1}{2}\frac{k\omega'\left(\omega + \omega'\right)}{k\omega'\omega + \mathrm{j}\left(\omega^2 - \omega'^2\right)}\begin{bmatrix} v_\alpha \\ v_\beta \end{bmatrix} \tag{8.64}$$

This transfer function describes the relationship between the amplitude of the positive-sequence component detected by the DSOGI and the actual amplitude of a given positive-sequence voltage vector applied to its input. This transfer function is plotted in the Bode diagram of Figure 8.22 as $P(j\omega) = |\boldsymbol{v}^+{}_{\alpha\beta}{}'|/|\boldsymbol{v}^+{}_{\alpha\beta}|$. By simply substituting ω by $-\omega$ in (8.64), another transfer function $N(j\omega) = |\boldsymbol{v}^+{}_{\alpha\beta}{}'|/|\boldsymbol{v}^-{}_{\alpha\beta}|$ can be defined. This second transfer function, also plotted in the *Bode* diagram of Figure 8.21, describes the relationship between the

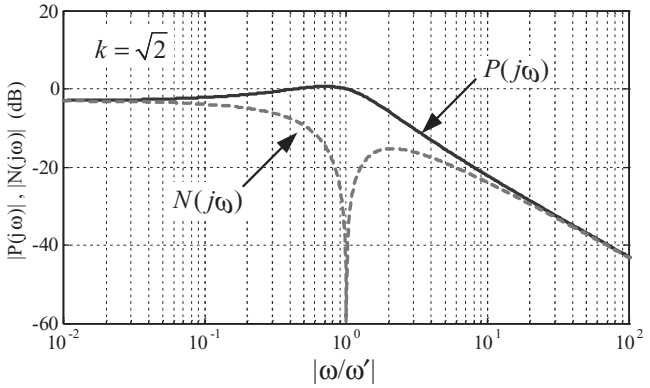

Figure 8.22 Frequency response of the DSOGI

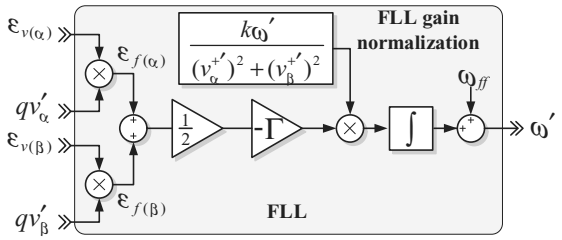

Figure 8.23 Structure of the FLL for the DSOGI.

detected amplitude for the positive-sequence component and the actual amplitude of a given negative-sequence voltage vector applied to the input of the DSOGI. As this *Bode* diagram shows, the DSOGI acts either as a low-pass filter or as a notch filter in the detection of the positive-sequence component, depending on whether the input voltage shows either a positive or a negative sequence respectively.

8.5.3 The FLL for the DSOGI

As presented in Section 4.6 of Chapter 4, a SOGI-QSG needs an FLL to become frequency adaptive. Moreover, the gain of the FLL has to be normalized in runtime according to the amplitude of the input signal in order to linearize the response of the frequency adaptation loop. Although mathematically correct, the use of two independent FLLs in the DSOGI-FLL might, however, seem conceptually odd since its two input signals, v_α and v_β, have the same frequency. For this reason, the DSOGI uses a single FLL (see Figure 8.23) in which the frequency error signals generated by the QSGs of the α and β signals have been combined by calculating an average error signal, i.e.

$$\varepsilon_f = \frac{\varepsilon_{f(\alpha)} + \varepsilon_{f(\beta)}}{2} = \frac{1}{2}\left(\varepsilon_\alpha q v'_\alpha + \varepsilon_\beta q v'_\beta\right) \tag{8.65}$$

The gain of this two-dimensional FLL is normalized by using the square of the amplitude of the positive-sequence component, i.e. $(v_\alpha^+)^2 + (v_\beta^+)^2$, which results in a first-order exponential linearized response with a settle time that still matches very well that one calculated by (4.109) in Chapter 4. In this manner, the DSOGI-FLL permits a decoupled estimation to be carried out of the symmetrical components of the input three-phase voltage on the $\alpha\beta$ reference frame, as well as the value of the grid frequency, something that is essential to implement power converter controllers on the stationary reference frame by using generalized integrators.

8.5.4 Response of the DSOGI-FLL

To evaluate the response of DSOGI-FLL the same unbalanced grid voltage as in the case of the DDSRF-PLL is applied to its input, i.e. a sag type C with $\vec{V}_a^{+1} = 0.5\angle -30^\circ$ and $\vec{V}_a^{-1} = 0.25\angle +60^\circ$. In this study case, the gain of the SOGI-QSGs was set to $k = \sqrt{2}$ to have the same tuning conditions as in the case of the evaluation of the DDSRF response ($\omega_f = \omega/\sqrt{2}$). The gain of the FLL was set to $\Gamma = 100$, which results in a settling time of around 45 ms according to the guidelines given in Section 4.6.1 of Chapter 4.

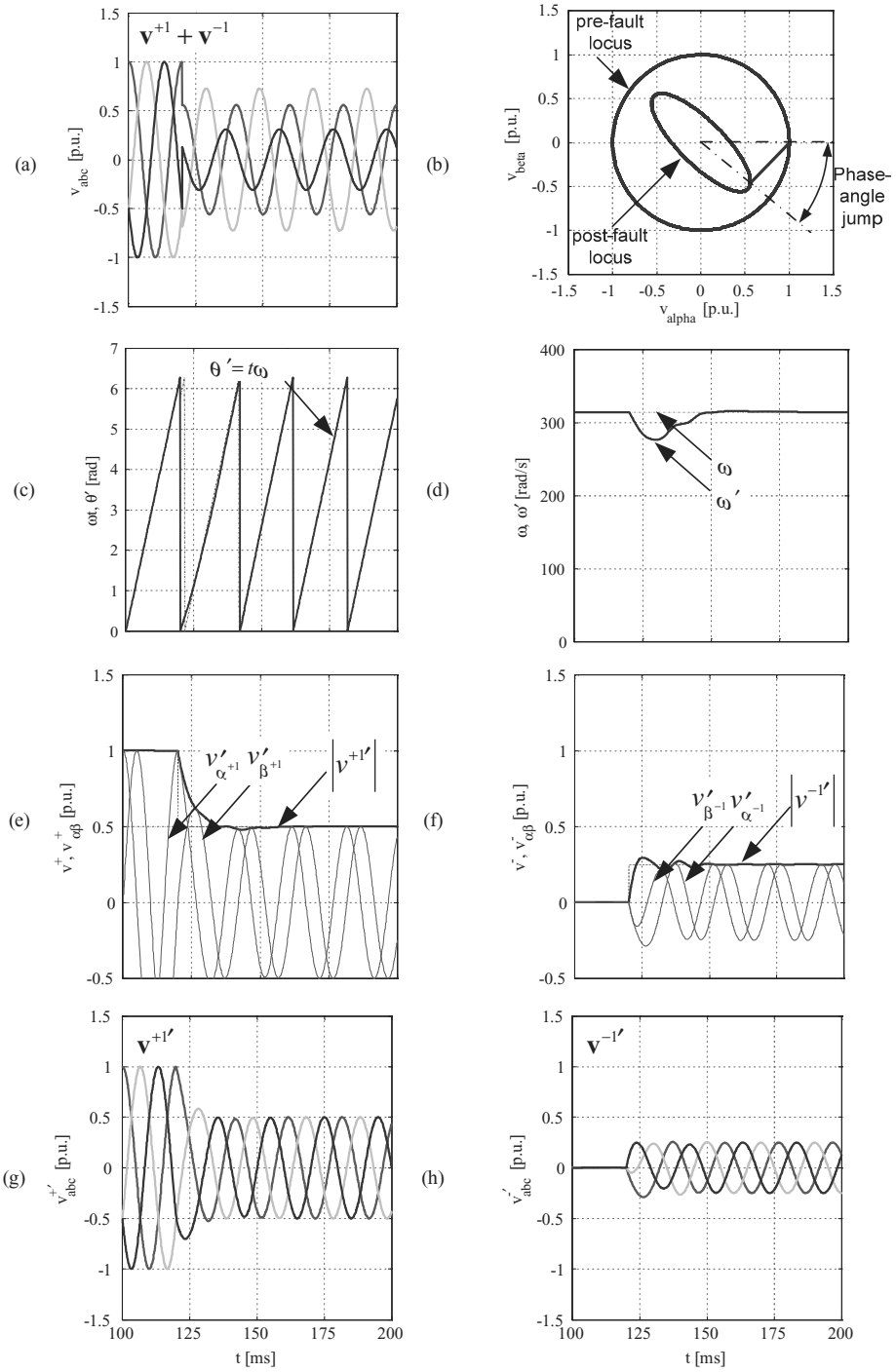

Figure 8.24 Representative waveforms of a DSOGI-FLL: (a) three-phase input voltage, (b) voltage vector locus, (c) detected phase angle, (d) detected frequency, (e) detected positive-sequence amplitude and $\alpha\beta$ signals, (f) detected negative-sequence amplitude and $\alpha\beta$ signals, (g) detected positive-sequence three-phase voltages and (h) detected negative-sequence three-phase voltages

The plot of Figure 8.24(a) shows the three-phase unbalanced voltages, which experience a jump in the phase angle as evidenced by the vector locus shown in Figure 8.24(b). The frequency detected by the FLL is shown in Figure 8.24(d). It is possible to appreciate in this figure how the detected frequency does not present high oscillations as in the case of the DDSRF-PLL. Moreover, the settling time in frequency adaptation matches the theoretical calculations. The amplitude and the phase angle of the sequence components detected by the DSOGI-FLL can be calculated by

$$\left|\boldsymbol{v}'\right| = \sqrt{\left(v'_{\alpha}\right)^2 + \left(v'_{\beta}\right)^2}; \quad \theta' = \tan^{-1}\frac{v'_{\beta}}{v'_{\alpha}} \tag{8.66}$$

The actual and the detected phase angle of the positive-sequence component of the unbalanced input voltage are plotted in Figure 8.24(c). This figure shows that the DSOGI-FLL completely cancels the steady-state error in the detected phase angle. Figure 8.24(e) shows the amplitude of the positive-sequence component together with the $\alpha\beta^{+1}$ signals. The amplitude of the negative-sequence component, together with the $\alpha\beta^{-1}$ signals are shown in Figure 8.24(f). The positive- and negative-sequence three-phase voltages can be reconstructed from the detected phase angle and amplitudes, and are shown in Figure 8.24(g) and (h).

After comparing the plots shown in Figures 8.20 and 8.24, it is possible to highlight the fact that the waveforms of the DSOGI-FLL are smoother than those of the DDSRF-PLL when the same unbalanced voltage is applied to their inputs and an equivalent set of parameters are used in both systems. This difference in the response of both synchronization systems gives rise to a significant divergence between the performances of power converter controllers working on the synchronous reference frame and on the stationary one, mainly when they operate under unbalanced grid faults.

8.6 Summary

This chapter has studied the characteristics of the three-phase voltage vector under unbalanced grid faults and presented expressions to determine its sequence components as a function of both the type of fault and the grid impedances.

The conventional SRF-PLL, although commonly used as a essential building block in the implementation of controllers for grid-connected converters, has demonstrated that it is not a suitable solution when a fast and precise grid synchronization is required during unbalanced grid faults, as is the case of the controllers for wind turbines and photovoltaics generators implementing the low-voltage ride-through functionality.

The DDSRF-PLL and the DSOGI-FLL, two advanced grid synchronization systems, have been presented in this chapter as suitable solutions to be used in the implementation of synchronous and stationary controllers for power converters respectively. The fundamental variable estimated by the DDSRF-PLL is the grid phase-angle, whereas the grid frequency is the one for the DSOGI-FLL. Since the grid frequency is a more stable variable than the grid phase-angle, the DSOGI-FLL use to present a smoother response than the DDSRF-PLL during transient faults.

References

[1] 'Towards Smart Power Networks – Lessons Learned from European Research FP5 Projects'. Luxembourg: European Commission – Office for Official Publications of the European Communities, Ref. EUR 21970, 2005.

[2] Dugan, R.C., McGranaghan, M.F., Santoso, S. and Beaty, H.W., *Electrical Power Systems Quality*, 2nd edition, New York: McGraw-Hill, 2002.

[3] Cichowlas, M., Malinowski, M., Sobczuk, D.L., Kazmierkowski, M. P., Rodríguez, P. and Pou, J., 'Active Filtering Function of Three-Phase PWM Boost Rectifier under Different Line Voltage Conditions'. *IEEE Transactions on Industrial Electronics*, **52**, April 2005, 410–419.

[4] Teodorescu, R. and Blaabjerg, F., 'Flexible Control of Small Wind Turbines with Grid Failure Detection Operating in Stand-alone and Grid-Connected Mode'. *IEEE Transactions on Power Electronics*, **19**, September 2004, 1323–1332.

[5] Nielsen, J. G., Newman, M., Nielsen, H. and Blaabjerg, F., 'Control and Testing of a Dynamic Voltage Restorer (DVR) at Medium Voltage Level'. *IEEE Transactions on Power Electronics*, **19**, May 2004, 806–813.

[6] Haque, M.H., 'Power Flow Control and Voltage Stability Limit: Regulating Transformer versus UPFC'. In *Proceedings of the IEE on Generation, Transmission and Distribution*, Vol. **151**, May 2004, pp. 299–304.

[7] Mattavelli, P., 'A Closed-Loop Selective Harmonic Compensation for Active Filters'. *IEEE Transactions on Industry Applications*, **37**, January/February 2001, 81–89.

[8] Bollen, M.H.J., *Understanding Power Quality Problems*, New York: IEEE Press, 2000.

[9] Bollen, M.H.J. and Gu, I., *Signal Processing of Power Quality Disturbances*, Wiley–IEEE Press, 2006. ISBN: 978-0-471-73168-9.

[10] Bollen, M.H.J. and Zhang, L. D., 'Different Methods for Classification of Three-Phase Unbalanced Voltage Dips Due to Faults'. *Electric Power Systems Research*, **66**(1), July 2003, 59–69.

[11] Fortescue, C.L., 'Method of Symmetrical Coordinates Applied to the Solution of Polyphase Networks'. *Transactions of AIEE*, Part II, **37**, 1918, 1027–1140.

[12] Joint Working Group JWG C4.110, 'Voltage Dip Immunity of Equipment Used in Installations', CIGRE/CIRED/UIE, http://www.jwgc4-110.org.

[13] Kaura, V. and Blasco, V., 'Operation of a Phase Locked Loop System under Distorted Utility Conditions'. *IEEE Transactions on Industry Applications*, **33**, January/February 1997, 58–63.

[14] Chung, S., 'A Phase Tracking System for Three Phase Utility Interface Inverters'. *IEEE Transactions on Power Electronics*, **15**, May 2000, 431–438.

[15] Timbus, A.V., Teodorescu, R., Blaabjerg, F., Liserre, M. and Rodriguez, P., 'PLL Algorithm for Power Generation Systems Robust to Grid Voltage Faults'. In *Proceedings of the Power Electronics Specialists Conference*, PESC '**06**, June 2006, pp. 1–7.

[16] McGrath, B. P., Holmes, D. G. and Galloway, J.J.H., 'Power Converter Line Synchronization Using a Discrete Fourier Transform (DFT) Based on a Variable Sample Rate'. *IEEE Transactions on Power Electronics*, **20**, July 2005, 877–884.

[17] Rodriguez, P., Pou, J., Bergas, J., Candela, J. I., Burgos, R.P. and Boroyevich, D., 'Decoupled Double Synchronous Reference Frame PLL for Power Converters Control'. *IEEE Transactions on Power Electronics*, **22**, March 2007, 584–592.

[18] Teodorescu, R., Blaabjerg, F., Liserre, M. and Loh, P., 'Proportional-Resonant Controllers and Filters for Grid-Connected Voltage-Source Converters'. *IEE Proceedings of Electrical Power Applications*, **153**, September 2006, 750–762.

[19] Zmood, D. and Holmes, D., 'Stationary Frame Current Regulation of PWM Inverters with Zero Steady-State Error'. *IEEE Transactions on Power Electronics*, **18**, May 2003, 814–822.

[20] Rodríguez, P., Bergas, J. and Gallardo, J.A., 'A New Positive Sequence Voltage Detector for Unbalanced Power Systems'. In *Proceedings of the European Conference on Power Electronics and Applications*, September 2002, CD Ref. T6-015.

[21] Rodriguez, P., Luna, A., Ciobotaru, M., Teodorescu, R. and Blaabjerg, F., 'Advanced Grid Synchronization System for Power Converters under Unbalanced and Distorted Operating Conditions'. In *IEEE Industrial Electronics (IECON 2006)*, 6–10 November 2006, pp. 5173–5178.

[22] Rodriguez, P., Luna, A., Candela, J. I., Rosas, R., Teodorescu, R. and Blaabjerg, F., 'Multi-Resonant Frequency-Locked Loop for Grid Synchronization of Power Converters under Distorted Grid Conditions'. *IEEE Transactions on Industrial Electronics*, **PP**(99), April 2010, 1.

[23] Anderson, P., 'Analysis of Faulted Power Systems'. In *IEEE Power, Energy, and Industry Applications*, 2009. ISBN 9780470544129.

[24] Lyon, W.V., *Application of the Method of Symmetrical Components*, New York: McGraw-Hill, 1937.